Large-Area Printed Metal Halide Perovskite Solar Cells

A Thesis

Presented to

the faculty of the School of Engineering and Applied Science

University of Virginia

---

in partial fulfillment
of the requirements for the degree

Doctor of Philosophy

by

Xiaoyu Deng

December 2019

APPROVAL SHEET

This Thesis
is submitted in partial fulfillment of the requirements
for the degree of
Doctor of Philosophy

Author Signature: ______________________

This Thesis has been read and approved by the examining committee:

Advisor: Joshua J. Choi

Committee Member: Gaurav Giri

Committee Member: Mool C. Gupta

Committee Member: Gary M. Koenig

Committee Member: Rachel A. Letteri

Committee Member: ______________________

Accepted for the School of Engineering and Applied Science:

Craig H. Benson, School of Engineering and Applied Science

December 2019

ABSTRACT

Metal halide perovskites (MHPs) are one of the most promising materials in solar industry. They are solution processed and have high light absorption coefficient and long electron-hole diffusion length. However, there are several current challenges to commercialize MHPs solar cells, one of which is that it is difficult to scale up the fabrication of MHPs thin film using the current spin coating, while roll-to-roll process is needed to fabricate solar cells on an industrial scale. Roll-to-roll process of perovskite solar cells can be achieved by overcoming the two challenges described below.

In the first part of the study, in order to achieve high-throughput roll-to-roll manufacturing of flexible perovskite solar cells, low temperature processing of all device layers are realized. The most commonly used electron transporting layer in high-performance perovskite solar cells are TiO_2 thin films and SnO_2 thin film processed at high temperature (450 °C and 180 °C respectively). Therefore, I designed the low temperature processes to fabricate these two kinds of metal oxide, TiO_x and SnO_2 thin film. Flexible solar cells fabricated with these thin films with decent power conversion efficiency are demonstrated.

In the second part, in order to achieve scalable fabrication of perovskite optoelectronic devices, large area deposition techniques such as solution shearing are realized. The mechanisms of fabrication processes are also studied in different solution shearing regimes. By monitoring the precursor species during crystallization process using In-situ Grazing Incidence Wide-Angle X-ray Scattering, the crystallization process in low shearing speed meniscus regime is proven to happen under lower supersaturation. The low supersaturation contributes to the bigger crystal size of thin film under lower shearing speed. Photodetectors with perovskite thin films coated at low shearing speed meniscus regime show much higher internal quantum efficiency because of the

larger crystal domain size and uniform orientation inside of domains. This shows continuing study and rational design of the crystallization process is needed to push perovskite technology toward useful applications.

TABLE OF COMTENTS

ABSTRACT **1**

NOMENCLATURE **6**

ACKNOWLEDGMENTS **7**

CHAPTER ONE. INTRODUCTION **9**

1.1 Motivation for solar cells 9

1.2 Introduction of three generations of solar cells 13

1.3 Perovskite solar cells and advantages 16

1.3.1 Structure 16

1.3.2 Development history 17

1.3.3 Advantages 17

1.4 Barrier to commercialization 18

1.4.1 Large scale fabrication method 18

1.4.2 Toxicity 20

1.5 Flexible solar cells 21

1.6 Solution shearing 21

1.7 Reference 24

CHAPTER TWO. ROOM TEMPERATURE PROCESSING OF TiO_x ELECTRON TRANSPORTING LAYER FOR PEROVSKITE SOLAR CELLS **33**

2.1 Abstract 33
2.2 Introduction 33
2.3 Results and Discussion 35
2.4 Methods 44
2.5 Supplementary Information 48
2.6 Reference 54
Chapter 3. Low-Temperature Processing of Tin Oxide Electron Transporting Layer for Flexible Perovskite Solar Cells 61
3.1 Abstract 61
3.2 Introduction 61
3.3 Results and discussion 63
3.4 Methods 69
3.5 Supplementary information 72
3.6 Reference 74
CHAPTER FOUR. MECHANISMS STUDY OF MENISCUS-GUIDED PEROVSKITE DEPOSITION FOR OPTOELECTRONIC DEVICES 81
4.1 Abstract 81
4.2 Introduction 81
4.3 Results and discussion 84
4.4 Methods 92

4.5 Supplement information 94

4.6 Reference 94

CHAPTER FIVE. CONCLUSION 100

NOMENCLATURE

DMAc	dimethylacetamide
DMF	dimethylformamide
ETL	electron transporting layer
FA+	formamidinium
FF	Fill Factor
FTO	fluorinated tin oxide
HTL	hole transporting layer
Isc	short circuit current
ITO	indium tin oxide
IV	current-voltage
Jsc	short circuit current density
MA+	methylammonium
MAPbI3	methylammonium lead iodide
MHPs	Metal Halide Perovskites
GIWAXS	grazing incidence wide angle X-ray scattering
Voc	open circuit voltage

ACKNOWLEDGMENTS

First and foremost, I would like to acknowledge my thesis advisor, Prof. Joshua Choi, for his guidance and encouragement over my PhD. His mentorship was essential in helping me develop as a scientist and be good at problem-solving, which are important skills for my future career development. He also trained me to be a writer and speaker, and teammate to others in the research group.

I would also like to thank my committee members for their support, particularly Prof. Giri for his support by sharing his synchrotron beam time and lab equipment and Prof. Gupta for the collaboration and guidance. I would also thank Dr. Detlef Smilgies for his assistance at the Cornell High Energy Synchrotron source.

All the members of Choi lab, Matt Alpert, Lucy Yoon, Katelyn Dagnall, Ashley Conley, Eric, and alumina Dr. Ben Foley, Dr. Alex Chen, Dr. Scott Niezgoda, have been an enormous help. I would like to thank them for their contributions to this work, maintaining the equipment, useful suggestions about my research, etc.

I would like to thank Giri lab members Stephanie Guthrie, Luke Huelsenbeck and Sangeun Steve Jung for helping me during synchrotron beam time and shearing lab equipment with me, especially Luke for his helping on building the shearing machine. I would also thank to Gupta lab members, Zeming Sun and George Wilks for collaborated projects. I would like to recognize undergraduate researchers Corner for his hard work.

I would like to thank my best friend Yuhong Yang, for her support during my hardest time and several visits to Charlottesville. I would thank Tong Yang for his crazy ideas, Qi Huang for his guidance on life, Yixing Liang for her company over phone calls. I would also thank my close friends Yinge Sun, Momo Ye, and Yiling Jia in Charlottesville, they have been great companies when I am far away from home.

Finally, I would like to thank my parents for their support throughout my PhD. I am grateful that they supported my decision of joining PhD program oversea even though I would be far away from home. They taught me to be a good person, have courage to pursue what I what, while to have no fear for failure because they are always there for me. I love you forever.

CHAPTER ONE. INTRODUCTION

Sine traditional (or fossil fuel based) energy is non-renewable and not environmentally friendly, solar energy is drawing more attention. Silicon solar cells have achieved high power conversion efficiency, however, high cost and rigidity limited their applications. Metal halide perovskites, with solution process ability and desired optical properties, have become one of the most promising new materials for solar cells. In order to commercialize perovskite solar cells, large-scale fabrication method is essential, which inspired this work.

1.1 Motivation for solar cells

Energy is essential for the development of society since it is a basic input for many productions and consumptions activities. The use of energy is essential for industrial growth, and a shortage of energy will have huge impact on economy. During 70's, Yom Kippur War and the Iranian Revolution interrupted oil exports in Middle Eastern. That lead to elevated prices of oil, which caused stagnant economic growth in many countries, such as the United States, Canada, Western Europe. For example, during this recession, the Gross Domestic Product (GPA) of the United States fell 3.2%. Since then, researchers began to pay attention to the correlation between energy and economy growth. Figure 1.1 shows that energy consumption has positive correlation with GPA.

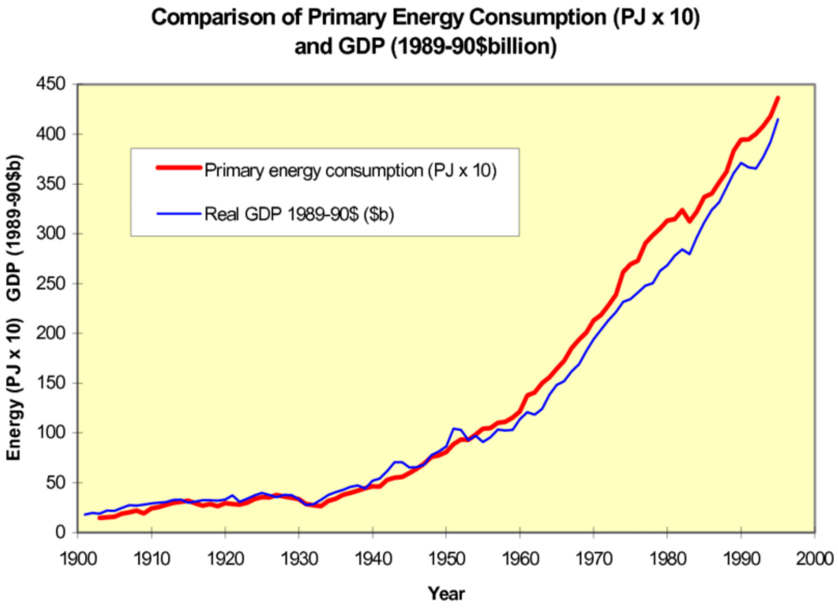

Figure 1.1 Correlation between energy consumption and GDP[1]

With the industrialization, the global energy consumption increased from 20×10^{18} J to more than 450×10^{18} J during last two hundred years, shown in Figure 1.2. However, there are only limited sources for traditional energy, including coal, oil, natural gas, nuclear, etc. which are also are referred as non-renewable energy. In future, the energy consumption rate will keep increasing and one day all the non-renewable energy will be exhausted. That is one of the reasons more researchers begin to explore renewable energy.

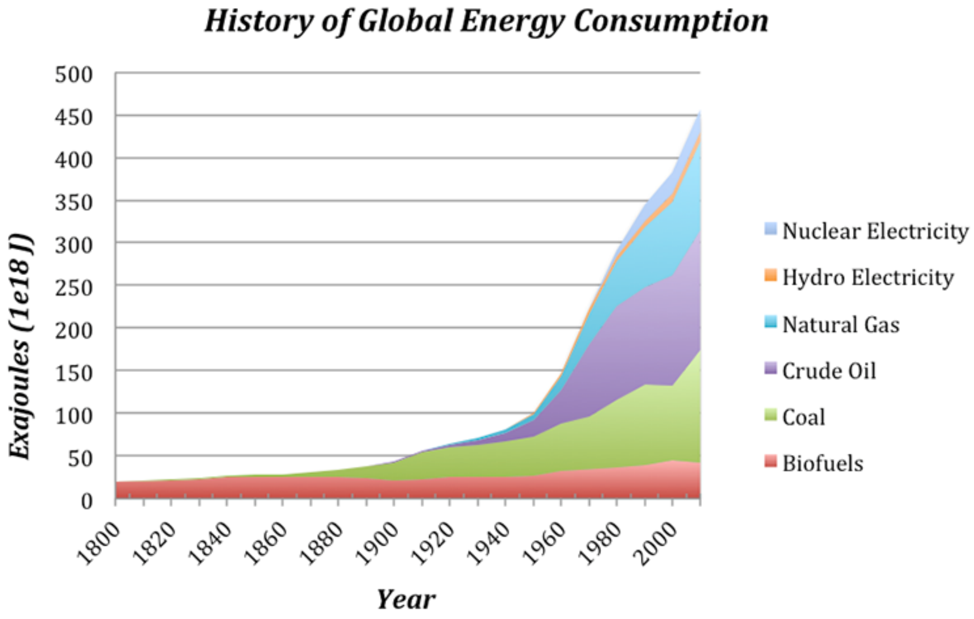

Figure 1.2 History of global energy consumption[2]

Another reason that people began to pay attention to renewable energy is that traditional energy also causes environmental problems. In the process of generating electricity from oil or coal, extremely large amounts of carbon dioxide is generated, which lead to green-house effect. The temperature of planet surface keep increasing, causing to melting of the iceberg, extinction of species, and abnormal weather conditions. Besides that, acid rain is also an important problem caused by sulfur and nitrogen oxides from burning coal and other fossil fuels. This atmospheric pollution will lead to the pollution to water system and destroy forests, which will have further negative effect on living organisms and ecosystem.

Traditional energy is not only non-renewable but also causes environmental problems as we introduced above. In order to solve these problems, people begin to study the renewable energy, such as sunlight, wind, rain, tides, waves and geothermal heat.[3] The categories of renewable and non-renewable energy resources are shown in Figure 1.3 below. Worldwide investments in renewable technologies is more than $286 billion in 2015[4]. Therefore, their contribution to global energy consumption is increasing dramatically.

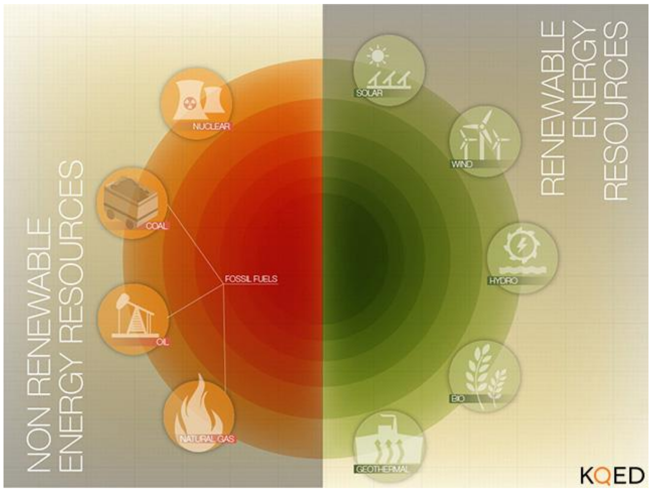

Figure 1.3 Category of renewable energy and non-renewable energy

Among renewable energy, wind and solar energy are the most popular ones. Solar energy has more application area considering the size of solar cells is much smaller compared with wind systems[5], for example, solar cells can easily be integrated onto house roof, road lamp and car top. Even though wind and solar have initial cost to set up in order to generate same electricity in 2018[6], wind system is more complicated and needs far higher ongoing maintenance costs than solar[7].

In this thesis, we will focus on using solar energy to generate electricity. First, current commercialized and academia development of solar cells will be introduced below.

1.2 Introduction of three generations of solar cells

In order to solve global energy problem, solar energy, as one of promising renewable energy, has drawn worldwide attention. Solar cells are able to transfer the solar energy into electricity. There are several generations of solar cells that have been studied and designed.

The first generation of solar cells is silicon solar cells, which is still the most efficient and popular solar cells available for now. The first silicon solar cell was reported in 1941 with less than 1% power conversion efficiency[8, 9]. After years of development, the power conversion efficiency increased dramatically to 27.8%[10]. The long-term stability over decades has also been proven in practice. However, silicon solar cells have low tolerance to raw material defects. The requirement for high-quality silicon wafer lead to high fabrication cost. Although the cost of crystalline silicon dropped a lot, the price of electricity generated by silicon solar cells is still not comparable with traditional fossil energy. Also, it is also impossible to fabricate rigid silicon substrate in to flexible solar cells.

In order to decrease high material usage and cost of silicon solar cells, the second generation solar cells have been introduced, which is also called thin film solar cells since the thickness of semiconductor layers are only a few micrometers thick. Thin film solar cells include copper indium gallium selenide (CIGS)[11, 12], cadmium telluride (CdTe)[13, 14], gallium arsenide (GaAs)[15] and amorphous silicon (a-Si:H)[16]. These solar cells have achieved high efficiency, almost comparable with commercialized silicon solar cell. For example, GaAs solar cells have achieved the highest performance, with efficiency of 28.8%[17] among all single-junction solar cells because its optimum bandgap of 1.42 eV. Even though these solar cells only require a thin film, most of the thin film solar cells are still expensive since they contain rare metals like tellurium and indium and toxic metal like cadmium, which limits their chance of scale up production. Amorphous silicon solar cell is less efficient and stable compared with other thin film solar cells.

In order to reduce the high cost of solar cells, there are lots of research going on about solar cells fabricated by advanced and less-commercialized materials, such as organic photovoltaics (OPVs)[18, 19], copper zinc tin sulphide (CZTS)[20, 21], dye-sensitised solar cells (DSSCs)[22, 23], quantum dot solar cells[24] and perovskite solar cells. Organic photovoltaics usually uses conductive polymers or organic small molecules. Even though it achieved low cost, flexibility, and easy to fabricate, efficiency limitation and long-term stability are still commercialization barriers. Other third generation solar cells have similar limitations except for perovskites solar cells. The efficiency chart will be used to show the points.

Figure 1.4 Three generation of solar cells

Shown in figure 1.5, expect for the multi-junction solar cells, which can take advantage of all the light along sunlight spectrum, single junction GaAs has the highest efficiency. However, the fabrication method of GaAs solar cells is complicated. Combining with the requirement of high material purity, it is expensive to fabricate, which limits the application in situations where cheap power is needed. Among all the third generation solar cells, shown as red circle with yellow face color, power conversion efficiency of perovskite solar cell has dramatically increased from less than five percent to more than twenty percent within seven years.

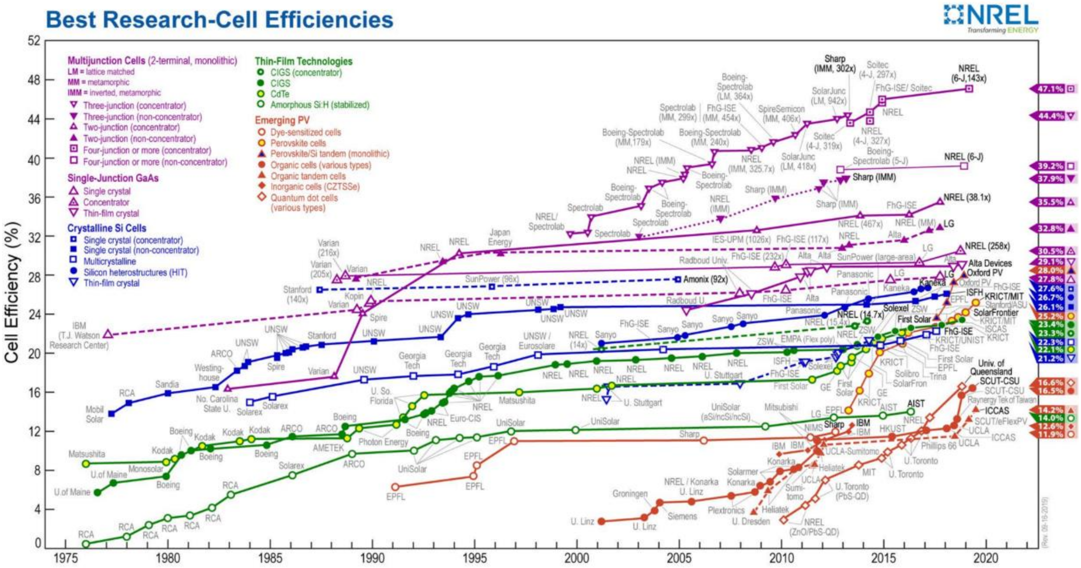

Fig 1.5 Power conversion efficiency of different generation[10]

Here, we will focus on perovskite solar cells considering they are one of the most promising new generations solar cells with straightforward fabrication method and low cost.

1.3 Perovskite solar cells and advantages

Metal halide perovskites (MHPs) are one of the most promising materials in solar industry. On the one hand, the cost of commercialized silicon-based solar cells has dropped precipitously in recent years, but its prices still cannot compete with conventional fossil-fuel based energy because of high-purity monocrystalline silicon wafers are needed to achieve high performance solar cells. On the other hand, the rigid silicon cells limit their applications, such as integration to curved surface or flexible screen. So, new generations of thin film solar cells have been studied as alternatives to silicon based solar cells. Among them, MHPs have attracted a lot of attention due to their rapid improvements in performance.

1.3.1 Structure

Perovskites adopt the chemical formula ABX_3, where A is n ion with a formal charge of +1(e.g. methylammonium (MA) $CH_3NH_3^+$; formamidinium (FA) $CH_3(NH_2)_2^+$), cesium Cs^+), B is divalent metal (e.g. Pb, Sn, Ge), and X is a halide[25]. Structure is shown in Figure 1.6.

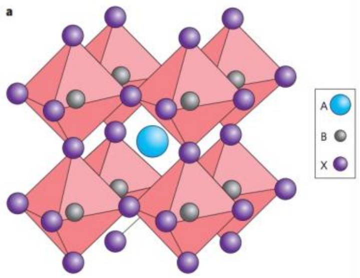

Figure 1.6 Structure of perovskites

1.3.2 Development history

The power conversion efficiency (PCE) of perovskite solar cells increases rapidly from 3.81%[26] to 23.3%[10] within several years, shown in Figure 1.5. In 2009, Miyasaka and colleagues achieved efficiency of 3.81% through employing $CH_3NH_3PbBr_3$ as sensitizers in liquid-electrolyte-based dye-sensitized solar cells.[26] Lee *et al.* replaced the mesoporous n-type TiO_2 with insulating Al_2O_3 and improved the power conversion efficiency.[27] Liu *et al.* has proven that nanostructuring is not necessary to achieve high efficiencies and fabricated a simple planar heterojunction solar cell with power conversion efficiencies of over 15 %.[28] The latest chart from National Renewable Energy Laboratory (NREL) shows the highest record PCE is 23.3%. [10]

1.3.3 Advantages

MHPs have plenty of advantages compared to silicon solar cells. They are is solution-processed, have high light absorbance coefficient and long electron-hole diffusion length.[29] They have an absorption coefficient of $1.5 \times 10^4\ \mathrm{cm}^{-1}$ at 550 nm, corresponding the penetration depth of 0.66 μm[30]. This makes the perovskite be able to absorb most incoming light with a thin film, which bears less strain when it is bent compared with thick films. Besides, polycrystalline perovskite solar cells with high efficiency can be fabricated. These factors allow lightweight flexible perovskite solar cells to be achieved, and further, make roll-to-roll process possible.

After several years of development, its remarkable performance and affordable fabrication process render it one of the most promising future renewable energy technologies.

1.4 Barrier to commercialization

More research needs to be done to commercialize MHPs solar cells, one aspect of it is that it is difficult to scale up the fabrication of MHPs thin films using the current laboratorial method. Now the perovskites solar cells with best performance were fabricated using the spin coating method.. However, spin coating method only can make uniform film with small area of only from several square millimeters to tens of centimeter, which is not suitable for industry fabrication process. Instead, roll-to-roll process, shown in Figure 1.7, is a commonly used industry technology to make large-area thin films because of the advantages of high precursor material utilization, saving storage room, easy transportation, and making uniform films with large area.[31, 32]

1.4.1 Large scale fabrication method

Roll-to-roll process of perovskite solar cells can be achieved by overcoming the following challenges. The first one is that all the thin films are need to be fabricated at low temperature since the substrates for flexible solar cells are usually plastics such as polyethylene naphthalate (PEN) or polyethylene terephthalate (PET). PEN and PET are transparent, lightweight, strong and safe, but they cannot withstand temperatures greater than 150 °C[33, 34]. Perovskite as light absorbing layer can be processed below 150 °C, while high temperature processes of metal oxides TiO_2 (500 °C) and SnO_2 (180 °C), commonly used as electron transporting layer (ETL) for MHPs solar cells are not compatible with flexible substrates. So fabrication processes for metal oxides at low temperature needs to be designed. Many previous efforts to deposit metal oxides at low temperature are based on vacuum-required processes, such as atom layer deposition (ALD)[35-38], electrodeposition[39-41], e-beam evaporation[42], which are not helpful with lowering cost. So facile sol-gel methods for both TiO_2 and SnO_2 have been studied in this thesis proposal.

Perovskite fabrication using large-area coating techniques need to be achieved in order to realize scaling up fabrication of solar cells. There are many large area coating methods, such as ink jet printing, spray coating, slot die coating, zone casting, blade coating, solution shearing etc.[43] For roll-to-roll process, different coating conditions, including different coating speed, temperature, gap width between blade and substrate, will lead to different coating regimes, then different crystal morphology and orientation. As we already know, uniform films with bigger crystal size and less surface defects will have lower election-hole recombination rate and better solar cells performance. Foley *et al.* showed that when grains of polycrystalline perovskite crystals have uniform crystallographic orientation and thus uniform surface termination, it has potential to achieve electronic uniformity comparable to single crystals[44]. Therefore, high degree of control over the crystallization process, especially morphology and crystallographic orientation of the thin film need to be achieved. Solution shearing will be chosen in this proposal since as it is compatible with roll to roll processing and allows for control of the crystallization process. Even though researchers began to fabricate MHPs solar cells using solution shearing method or similar processes during recent two years[45-50], fundamental understanding of perovskite crystal nucleation and growth during solution shearing process is not available yet, so how to control crystallization by controlling coating conditions has not been understood.

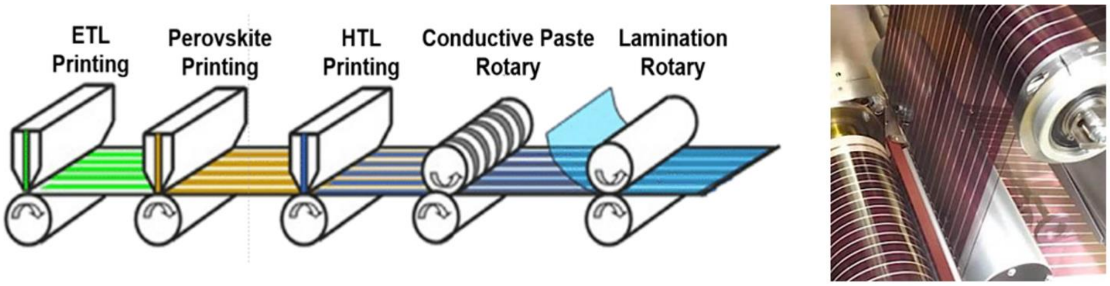

Figure 1.7 Scaled-up MHPs flexible solar cells fabricated by roll-to-roll process

1.4.2 Toxicity

Another problem is that the perovskites currently used for solar cells contain lead, which is a highly poisonous metal. For future use, it needs encapsulation which would raise its price. So researchers are working on replacing lead with other divalent metallic cations. According to the Shockley–Queisser limit[7], the optimal bandgap for solar cells is 1.34 eV, meaning the bandgap of a new material should be around there. Hao *et al.* has found PSC based on the $CH_3NH_3SnI_3$ perovskite, with an optical bandgap of 1.3 eV, shows a PCE of 5.23%[8]. However, Sn^{+2} is really unstable and can be oxidized into Sn^{+4} easily in the air. Stoumpos *et al.* synthesized a series of Ge-based perovskites, including $CsGeI_3$, $CH_3NH_3GeI_3$ etc. with band gaps of 1.6 eV, 1.9 eV separately[9]. However, the solar cells based on them have efficiency of below 1% because of poor film forming abilities and oxidizing tendencies[10]. There are a large number of possible combinations of divalent metals and halides, and Density Functional Theory (DFT) calculations can be used to suggest promising materials. Filip *et al.* has done systematic research into the bandgap of lead free perovskites[11]. The bandgap of all ABX_3 compounds based on +2 oxidation state metal ion were calculated using DFT, and compounds with bandgap over 3.5 eV were discarded. Then the materials without stable perovskite structure were excluded. Finally, the bandgap threshold was lowered from 3.5 eV to 2 eV in order to refine the result and Mg, Mn, V, and Ni were left as potential candidate to replace Pb in perovskites. Based on these simulation results, experiment can be executed to explore possible non-toxic perovskite material suit for solar cells.

1.5 Flexible solar cells

As we discussed above, flexible solar cells are necessary because it is compatible with roll to roll process. Besides that, flexible solar cells also have other advantages motivating researchers to study the fabrication process on flexible substrates.

Flexible solar cells are easier and cheaper to transport and store because they are thinner, light in weight, and especially bendable, while rigid solar cells are thicker and heavier[51]. This make it possible to decrease related cost. The flexibility makes them can be integrated all kinds of surface, such as car top, backpack, clothes, even portable light-weight phone charger, etc. shown in Figure 1.9. Furthermore, it can be used in flights or space applications since it is light in weight.

Figure 1.8 Applications of flexible solar cells

1.6 Solution shearing

In this project, we will focus on solving the first challenge of commercializing perovskite solar cells, scale up fabrication. As we discussed above, a large-scale thin film fabrication method for solution process is needed, for example, solution shearing.

Although some researchers began to fabricate perovskite solar cells using solution shearing[45-50], almost none of them studied the crystallization of perovskite during solution shearing process.

However, fundamental knowledge is necessary to understand how to control the crystallization of perovskite during solution shearing. Studies on perovskite solution shearing can base on fundamental studies on solution shearing or similar processes (dip coating etc.) for other materials, such as polymer or organic small molecules[52, 53].

For solution shearing in certain solution systems, with liquid viscosity and surface tension being the same, coating speed is one of the most important variables. When coating speed is sufficiently high, evaporation rate is significantly slower than the coating speed, so a liquid thin film will be dragged out first on substrates by viscous forces. In this situation, crystallization happens far away from solution meniscus, which is known as Landau-Levich (LL) regime[54] shown in Figure 1.9 (left). In LL regime, blade moving is decoupled with solvent evaporation and crystallization, so molecules in liquid film dragged out first have enough time to relax from shearing stress before solvent evaporation, leading to less control of crystallization performed by coating process. When coating speed is sufficiently low enough such that, crystallization mainly happens in the solution meniscus, evaporative regime shown in Figure 1.9 (right) occurs[55-58]. In this regime, the solvent evaporation and crystallization happen in the similar time scale, which leads to solute crystalizes under shearing stress in meniscus, providing additional ways to control crystallization. So coating in evaporative regime is called meniscus-guided deposition.

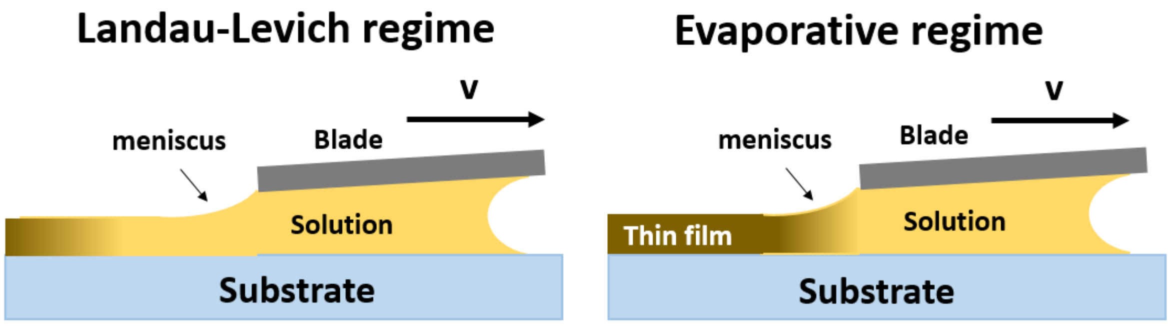

Figure 1.9 Graph of evaporative regime and Landau-Levich regime.

There are many studies showed that the crystallization control is able to achieve under shearing stress in the evaporative regime. Leo Shaw *et al.* achieved oriented donor-acceptor semiconducting polymer thin film at low coating speed[52]. They claimed most of the oriented nucleation happens in liquid-substrate surface under shear stress at low coating speed, which induces the growth of the oriented polymer thin film. Increasing coating speed will induce nucleation at air-liquid interface with random orientation and higher density, even though the nucleation from air-liquid interface sometimes also can achieve oriented thin film in some cases[59-63]. Except for polymers, oriented thin films of different materials can also be achieved by coating in evaporative regime. Gaurav Giri *et al.* shown metastable polymorph can be achieved by the spatial confinement of equilibrium polymorph crystalized on the air-liquid interface in meniscus[64]. Steve park *et al.* shown densely aligning single-walled carbon nanotubes can be fabricated through meniscus confinement[65]. Ying Diao *et al.* achieved highly aligned single organic semiconductor thin films with high coating speed. This is because they patterned blade with micro-pillars and substrate with solvent wetting and non-wetting region[66]. These studies show that meniscus guided deposition can realize good control of crystallization and obtain thin films with desired properties.

There are several papers that reported the authors achieved the special morphology and properties for perovskite crystallized in evaporative regime. Compact and oriented perovskite thin films were fabricated at low shearing speed[47, 49]. Even though control of crystal morphology has been achieved, fundamental understanding of crystallization process need to be explored more.

In this work, we will focus on solving the first barriers for commercializing perovskite solar cells, scaling up the fabrication process of perovskite solar cell. Condensing roll-to-roll process is a commonly used large-scale fabrication method for solution process, there would be two challenges need to overcome. Therefore, the goal for this project is divided into two parts. One is to fabricate perovskite solar cells on flexible substrates, and another is to understand the mechanism to fabricate perovskite thin film using solution shearing method in order to coat large area of perovskite thin film with desired properties.

1.7 Reference

1. M. Dunlop, G. Turner, B. Foran, and F. Poldy, *Decision points for land and water futures*. 2002.
2. World Energy Consumption Since 1820 in Charts: https://ourfiniteworld.com/2012/03/12/world-energy-consumption-since-1820-in-charts/,
3. O. Ellabban, H. Abu-Rub, and F. Blaabjerg, Renewable energy resources: Current status, future prospects and their enabling technology, Renewable and Sustainable Energy Reviews 39 (2014) 748-764.
4. Renewables added more to global energy generation capacity than all other technologies combined, UN-backed report finds, Sustainable development goals (2016)
5. L. Cameron and B. van der Zwaan, Employment factors for wind and solar energy technologies: A literature review, Renewable and Sustainable Energy Reviews 45 (2015) 160-172.

6. International Renewable Energy Agency (IRENA): https://www.irena.org/publications/2019/May/Renewable-power-generation-costs-in-2018,

7. M. Shafiee, Maintenance logistics organization for offshore wind energy: Current progress and future perspectives, Renewable Energy 77 (2015) 182-193.

8. Ohl RS. Light sensitive electric device. US Patent240252, filed 27 March 1941. ,

9. Light-sensitive electricdevice including silicon. US Patent 2443542, filed 27May 1941.,

10. N.R.C.R.E.C. https://www.nrel.gov/pv/assets/images/efficiency-chart-20180716.jpg,

11. S.S. N. Naghavi, M. Powalla, B. Cavana, D. Lincot, High‐efficiency copper indium gallium diselenide (CIGS) solar cells with indium sulfide buffer layers deposited by atomic layer chemical vapor deposition (ALCVD), Progress in Photovoltaics: Research and Applications 11 (2003) 437-443.

12. T.B. Harvey, I. Mori, C.J. Stolle, T.D. Bogart, D.P. Ostrowski, M.S. Glaz, J. Du, D.R. Pernik, V.A. Akhavan, H. Kesrouani, D.A. Vanden Bout, and B.A. Korgel, Copper indium gallium selenide (CIGS) photovoltaic devices made using multistep selenization of nanocrystal films, ACS Appl Mater Interfaces 5 (2013) 9134-40.

13. S.S.C. T.L. Chu, J. Britt, C. Ferekides, C. Wang, C.Q. Wu, H.S. Ullal 14.6% efficient thin-film cadmium telluride heterojunction solar cells, IEEE Electron Device Letters 13 (1992) 303-304.

14. K. Zweibel, The Impact of Tellurium Supply on Cadmium Telluride Photovoltaics, Science 7 (2010) 699-701.

15. J. Wang, A. Santamato, P. Jiang, D. Bonneau, E. Engin, J.W. Silverstone, M. Lermer, J. Beetz, M. Kamp, S. Höfling, M.G. Tanner, C.M. Natarajan, R.H. Hadfield, S.N. Dorenbos,

V. Zwiller, J.L. O’Brien, and M.G. Thompson, Gallium arsenide (GaAs) quantum photonic waveguide circuits, Optics Communications 327 (2014) 49-55.

16. D.E. Carlson and C.R. Wronski, Amorphous silicon solar cell, Appl. Phys. Lett. 28 (1976) 671-673.

17. M.A. Green, Y. Hishikawa, E.D. Dunlop, D.H. Levi, J. Hohl-Ebinger, M. Yoshita, and A.W.Y. Ho-Baillie, Solar cell efficiency tables (Version 53), Progress in Photovoltaics: Research and Applications 27 (2019) 3-12.

18. B. Kippelen and J.-L. Brédas, Organic photovoltaics, Energy Environ. Sci. 2 (2009) 251.

19. C.J. Brabec, Organic photovoltaics: technology and market, Sol. Energy Mater. Sol. Cells 83 (2004) 273-292.

20. V. Kheraj, K.K. Patel, S.J. Patel, and D.V. Shah, Synthesis and characterisation of Copper Zinc Tin Sulphide (CZTS) compound for absorber material in solar-cells, J. Cryst. Growth 362 (2013) 174-177.

21. X. Xin, M. He, W. Han, J. Jung, and Z. Lin, Low-cost copper zinc tin sulfide counter electrodes for high-efficiency dye-sensitized solar cells, Angew. Chem. Int. Ed. Engl. 50 (2011) 11739-42.

22. I. Kartini, D. Menzies, D. Blake, J.C.D. da Costa, P. Meredith, J.D. Riches, and G.Q. Lu, Hydrothermal seeded synthesis of mesoporous titania for application in dye-sensitised solar cells (DSSCs), J. Mater. Chem. 14 (2004) 2917.

23. J. Preat, D. Jacquemin, and E.A. Perpète, Towards new efficient dye-sensitised solar cells, Energy Environ. Sci. 3 (2010) 891.

24. A.JNozik, Quantum dot solar cells, Physica E: Low-dimensional Systems and Nanostructures 14 (2002) 115-120.

25. N.-G. Park, Perovskite solar cells: an emerging photovoltaic technology, Materials Today 18 (2015) 65-72.

26. A. Kojima, K. Teshima, Y. Shirai, and T. Miyasaka, Organometal Halide Perovskites as Visible-Light Sensitizers for Photovoltaic Cells, J. Am. Chem. Soc. 131 (2009) 6050-6051.

27. J.T. Michael M. Lee, Tsutomu Miyasaka, Takurou N. Murakami, Henry J. Snaith, Efficient Hybrid Solar Cells Based on Meso-Superstructured Organometal Halide Perovskites, Science 338 (2012) 643-647.

28. M. Liu, M.B. Johnston, and H.J. Snaith, Efficient planar heterojunction perovskite solar cells by vapour deposition, Nature 501 (2013) 395-8.

29. M. Nakamura, S. Kato, T. Aoki, L. Sirghi, and Y. Hatanaka, Role of terminal OH groups on the electrical and hydrophilic properties of hydro-oxygenated amorphous TiOx:OH thin films, J. Appl. Phys. 90 (2001) 3391-3395.

30. S.H. Park, A. Roy, S. Beaupré, S. Cho, N. Coates, J.S. Moon, D. Moses, M. Leclerc, K. Lee, and A.J. Heeger, Bulk heterojunction solar cells with internal quantum efficiency approaching 100%, Nat. Photon. 3 (2009) 297-302.

31. C. Zuo, D. Vak, D. Angmo, L. Ding, and M. Gao, One-step roll-to-roll air processed high efficiency perovskite solar cells, Nano Energy 46 (2018) 185-192.

32. B.J. Foley, S. Cuthriell, S. Yazdi, A.Z. Chen, S.M. Guthrie, X. Deng, G. Giri, S.-H. Lee, K. Xiao, B. Doughty, Y.-Z. Ma, and J.J. Choi, Impact of Crystallographic Orientation Disorders on Electronic Heterogeneities in Metal Halide Perovskite Thin Films, Nano Lett. 18 (2018) 6271-6278.

33. G.S. Han, S. Lee, M.L. Duff, F. Qin, and J.K. Lee, Highly Bendable Flexible Perovskite Solar Cells on a Nanoscale Surface Oxide Layer of Titanium Metal Plates, ACS Appl Mater Interfaces 10 (2018) 4697-4704.

34. K. Li, J. Xiao, X. Yu, T. Li, D. Xiao, J. He, P. Zhou, Y. Zhang, W. Li, Z. Ku, J. Zhong, F. Huang, Y. Peng, and Y. Cheng, An efficient, flexible perovskite solar module exceeding 8% prepared with an ultrafast PbI2 deposition rate, Sci Rep 8 (2018) 442.

35. A.K. Chandiran, A. Yella, M.T. Mayer, P. Gao, M.K. Nazeeruddin, and M. Gratzel, Sub-nanometer conformal TiO2 blocking layer for high efficiency solid-state perovskite absorber solar cells, Adv. Mater. 26 (2014) 4309-12.

36. B.J. Kim, D.H. Kim, Y.-Y. Lee, H.-W. Shin, G.S. Han, J.S. Hong, K. Mahmood, T.K. Ahn, Y.-C. Joo, K.S. Hong, N.-G. Park, S. Lee, and H.S. Jung, Highly efficient and bending durable perovskite solar cells: toward a wearable power source, Energy Environ. Sci. 8 (2015) 916-921.

37. C. Wang, L. Guan, D. Zhao, Y. Yu, C.R. Grice, Z. Song, R.A. Awni, J. Chen, J. Wang, X. Zhao, and Y. Yan, Water Vapor Treatment of Low-Temperature Deposited SnO2 Electron Selective Layers for Efficient Flexible Perovskite Solar Cells, ACS Energy Lett. 2 (2017) 2118-2124.

38. C. Wang, D. Zhao, C.R. Grice, W. Liao, Y. Yu, A. Cimaroli, N. Shrestha, P.J. Roland, J. Chen, Z. Yu, P. Liu, N. Cheng, R.J. Ellingson, X. Zhao, and Y. Yan, Low-temperature plasma-enhanced atomic layer deposition of tin oxide electron selective layers for highly efficient planar perovskite solar cells, J. Mater. Chem. A 4 (2016) 12080-12087.

39. J.-Y. Chen, C.-C. Chueh, Z. Zhu, W.-C. Chen, and A.K.Y. Jen, Low-temperature electrodeposited crystalline SnO 2 as an efficient electron-transporting layer for conventional perovskite solar cells, Sol. Energy Mater. Sol. Cells 164 (2017) 47-55.

40. J. Zhang, E.J. Juárez-Pérez, I. Mora-Seró, B. Viana, and T. Pauporté, Fast and low temperature growth of electron transport layers for efficient perovskite solar cells, J. Mater. Chem. A 3 (2015) 4909-4915.

41. J.-Y. Lam, J.-Y. Chen, P.-C. Tsai, Y.-T. Hsieh, C.-C. Chueh, S.-H. Tung, and W.-C. Chen, A stable, efficient textile-based flexible perovskite solar cell with improved washable and deployable capabilities for wearable device applications, RSC Adv. 7 (2017) 54361-54368.

42. W. Qiu, U.W. Paetzold, R. Gehlhaar, V. Smirnov, H.-G. Boyen, J.G. Tait, B. Conings, W. Zhang, C.B. Nielsen, I. McCulloch, L. Froyen, P. Heremans, and D. Cheyns, An electron beam evaporated TiO2layer for high efficiency planar perovskite solar cells on flexible polyethylene terephthalate substrates, J. Mater. Chem. A 3 (2015) 22824-22829.

43. Y. Diao, L. Shaw, Z. Bao, and S.C.B. Mannsfeld, Morphology control strategies for solution-processed organic semiconductor thin films, Energy Environ. Sci. 7 (2014) 2145-2159.

44. B.J. Foley, S. Cuthriell, S. Yazdi, A.Z. Chen, S.M. Guthrie, X. Deng, G. Giri, S.H. Lee, K. Xiao, B. Doughty, Y.Z. Ma, and J.J. Choi, Impact of Crystallographic Orientation Disorders on Electronic Heterogeneities in Metal Halide Perovskite Thin Films, Nano Lett (2018)

45. Y. Deng, Q. Wang, Y. Yuan, and J. Huang, Vividly colorful hybrid perovskite solar cells by doctor-blade coating with perovskite photonic nanostructures, Materials Horizons 2 (2015) 578-583.

46. M. Yang, Z. Li, M.O. Reese, O.G. Reid, D.H. Kim, S. Siol, T.R. Klein, Y. Yan, J.J. Berry, M.F.A.M. van Hest, and K. Zhu, Perovskite ink with wide processing window for scalable high-efficiency solar cells, Nature Energy 2 (2017) 17038.

47. J. Li, Y. Liu, X. Ren, Z. Yang, R. Li, H. Su, X. Yang, J. Xu, H. Xu, J.-Y. Hu, A. Amassian, K. Zhao, and S.F. Liu, Solution Coating of Superior Large-Area Flexible Perovskite Thin Films with Controlled Crystal Packing, Advanced Optical Materials 5 (2017) 1700102.

48. Y. Deng, Q. Dong, C. Bi, Y. Yuan, and J. Huang, Air-Stable, Efficient Mixed-Cation Perovskite Solar Cells with Cu Electrode by Scalable Fabrication of Active Layer, Advanced Energy Materials 6 (2016) 1600372.

49. M. He, B. Li, X. Cui, B. Jiang, Y. He, Y. Chen, D. O'Neil, P. Szymanski, M.A. Ei-Sayed, J. Huang, and Z. Lin, Meniscus-assisted solution printing of large-grained perovskite films for high-efficiency solar cells, Nat Commun 8 (2017) 16045.

50. H. Wu, C. Zhang, K. Ding, L. Wang, Y. Gao, and J. Yang, Efficient planar heterojunction perovskite solar cells fabricated by in-situ thermal-annealing doctor blading in ambient condition, Organic Electronics 45 (2017) 302-307.

51. D. Yang, R. Yang, S. Priya, and S.F. Liu, Recent Advances in Flexible Perovskite Solar Cells: Fabrication and Applications, Angew. Chem. Int. Ed. Engl. 58 (2019) 4466-4483.

52. L. Shaw, H. Yan, X. Gu, P. Hayoz, R.T. Weitz, D. Kaelblein, M.F. Toney, and Z. Bao, Microstructural Evolution of the Thin Films of a Donor–Acceptor Semiconducting Polymer Deposited by Meniscus-Guided Coating, Macromolecules 51 (2018) 4325-4340.

53. H. Yang and P. Jiang, Large-scale colloidal self-assembly by doctor blade coating, Langmuir 26 (2010) 13173-82.

54. R.L. Davis, S. Jayaraman, P.M. Chaikin, and R.A. Register, Creating controlled thickness gradients in polymer thin films via flowcoating, Langmuir 30 (2014) 5637-44.

55. G. Jing, H. Bodiguel, F. Doumenc, E. Sultan, and B. Guerrier, Drying of colloidal suspensions and polymer solutions near the contact line: deposit thickness at low capillary number, Langmuir 26 (2010) 2288-93.

56. F. Doumenc, J.B. Salmon, and B. Guerrier, Modeling Flow Coating of Colloidal Dispersions in the Evaporative Regime: Prediction of Deposit Thickness, Langmuir 32 (2016) 13657-13668.

57. R. Janneck, F. Vercesi, P. Heremans, J. Genoe, and C. Rolin, Predictive Model for the Meniscus-Guided Coating of High-Quality Organic Single-Crystalline Thin Films, Adv Mater 28 (2016) 8007-8013.

58. C. Loussert, F. Doumenc, J.B. Salmon, V.S. Nikolayev, and B. Guerrier, Role of Vapor Mass Transfer in Flow Coating of Colloidal Dispersions in the Evaporative Regime, Langmuir 33 (2017) 14078-14086.

59. T. Kushida, T. Nagase, and H. Naito, Air-mediated self-organization of polymer semiconductors for high-performance solution-processable organic transistors, Applied Physics Letters 98 (2011) 063304.

60. T. Schuettfort, L. Thomsen, and C.R. McNeill, Observation of a distinct surface molecular orientation in films of a high mobility conjugated polymer, J Am Chem Soc 135 (2013) 1092-101.

61. Q. Wei, S. Miyanishi, K. Tajima, and K. Hashimoto, Enhanced charge transport in polymer thin-film transistors prepared by contact film transfer method, ACS Appl Mater Interfaces 1 (2009) 2660-6.

62. Q. Wei, K. Tajima, and K. Hashimoto, Electrical instability of polymer thin-film transistors using contact film transfer methods, Applied Physics Letters 96 (2010) 243301.

63. D. Wu, M. Kaplan, H.W. Ro, S. Engmann, D.A. Fischer, D.M. DeLongchamp, L.J. Richter, E. Gann, L. Thomsen, C.R. McNeill, and X. Zhang, Blade Coating Aligned, High-Performance, Semiconducting-Polymer Transistors, Chemistry of Materials 30 (2018) 1924-1936.

64. G. Giri, R. Li, D.M. Smilgies, E.Q. Li, Y. Diao, K.M. Lenn, M. Chiu, D.W. Lin, R. Allen, J. Reinspach, S.C. Mannsfeld, S.T. Thoroddsen, P. Clancy, Z. Bao, and A. Amassian, One-dimensional self-confinement promotes polymorph selection in large-area organic semiconductor thin films, Nat Commun 5 (2014) 3573.

65. S. Park, G. Pitner, G. Giri, J.H. Koo, J. Park, K. Kim, H. Wang, R. Sinclair, H.S. Wong, and Z. Bao, Large-area assembly of densely aligned single-walled carbon nanotubes using solution shearing and their application to field-effect transistors, Adv Mater 27 (2015) 2656-62.

66. Y. Diao, B.C. Tee, G. Giri, J. Xu, D.H. Kim, H.A. Becerril, R.M. Stoltenberg, T.H. Lee, G. Xue, S.C. Mannsfeld, and Z. Bao, Solution coating of large-area organic semiconductor thin films with aligned single-crystalline domains, Nat Mater 12 (2013) 665-71.

CHAPTER TWO. ROOM TEMPERATURE PROCESSING OF TiO_x ELECTRON TRANSPORTING LAYER FOR PEROVSKITE SOLAR CELLS

This chapter was published as: J. Phys. Chem. Lett. 2017, 8, 14, 3206-3210

2.1 Abstract

In order to realize high-throughput roll-to-roll manufacturing of flexible perovskite solar cells, low temperature processing of all device components must be realized. However, the most commonly used electron transporting layer is based on TiO_2 thin films processed at high temperature (>450 °C). Here, we demonstrate room temperature solution processing of the TiO_x layer that performs as well as the high temperature TiO_2 layer in perovskite solar cells, as evidenced by a champion solar cell efficiency of 16.3%. Using optical spectroscopy, electrical measurements, and X-ray diffraction, we show that the room temperature processed TiO_x is amorphous with organic residues and yet its optical and electrical properties are on par with the high temperature TiO_2. Flexible perovskite solar cells that employ a room temperature TiO_x layer with a power conversion efficiency of 14.3% are demonstrated.

2.2 Introduction

Metal halide perovskite (MHP) solar cells have demonstrated the most rapid improvement in power conversion efficiency (PCE) among all photovoltaic technologies to date. With a record

PCE of 22.1%[1], MHP solar cells are now on par with silicon solar cells in terms of efficiency. Moreover, MHP solar cells can be fabricated entirely using low-cost solution processing methods and earth-abundant compositions. Therefore, they can combine high efficiency with low cost and have a great potential for realizing more economically competitive solar power.

What is particularly exciting about MHPs is that they can be deposited on various substrates at low temperature (<150 ºC) and enable roll-to-roll manufacturing of low-cost, lightweight and flexible devices[2]. Lead halide-based MHPs have been shown to possess a large extinction coefficient greater than 10^4 cm^{-1}, and a long electron-hole diffusion length in the range of hundreds of nanometers to microns in polycrystalline thin films[3]. This means that a film only about 500 nm thick can harvest most of the sunlight and efficiently transport the photogenerated charges into the external circuit. Such a thin MHP film is highly flexible and corresponds to only 2 g/m^2 of weight which is two orders of magnitude lighter than a silicon solar cell. Successful development of MHP solar cells that simultaneously combine high efficiency, low cost, light weight, and flexibility can enable novel portable power generation capabilities in situations where conventional rigid and heavy solar cells are not feasible, such as wearable electronics, solar aviation, automobiles, building integrated photovoltaics, and more.

While the quest for achieving high PCE has shown exceptional progress, a majority of the high-performance MHP solar cell structures rely on a titanium dioxide (TiO_2) electron transporting layer (ETL) processed at high temperatures (>450 °C). The high temperature requirement prohibits the use of flexible plastic substrates such as polyethylene terephthalate (PET) and polyethylene naphthalate (PEN) that cannot withstand temperatures greater than 150 °C. Due to the high performance of metal oxide-based ETLs for MHP solar cells, it is of great interest to achieve low-temperature processing of metal oxide thin films with favorable optical and electrical properties.

Indeed, among all flexible MHP solar cell results to date, device architectures that employ metal oxide ETLs currently hold the best PCE records of between 15% and 18%[4-6]. Previous efforts to deposit metal oxide ETLs on flexible substrates at low temperature have been based on solution processing of nanoparticles[5, 7-13], sputter deposition[4, 14, 15], spray coating[16, 17], e-beam evaporation[18], atomic layer deposition (ALD) [19, 20], and electrodeposition[21, 22]. Despite the encouraging device performance, these methods require vacuum processing steps, nanoparticle formulations, etc., that can significantly increase the cost while reducing the throughput. Therefore, there is a need for developing low-temperature solution processing of metal oxide films starting from simple and low-cost commercially available precursors.

Here, we demonstrate that room temperature processing of simple solution formulation (titanium (IV) isopropoxide ($Ti(OiPr)_4$) in isopropanol) can result in a TiO_x layer with high performance in MHP solar cells, as evidenced by a champion solar cell efficiency of 16.3%. Using optical spectroscopy, electrical measurements, and X-ray diffraction, we show that the room temperature processed TiO_x is amorphous with organic residues and yet its optical and electrical properties are on par with the high temperature TiO_2. Flexible MHP perovskite solar cells with a power conversion efficiency of 14.3% were achieved with the room temperature processed TiO_x layer. The power conversion efficiency could potentially be increased further through process optimization.

2.3 Results and Discussion

The room temperature (RT) processed thin films from the $Ti(OiPr)_4$ solution, from here on referred to as "$Ti(OiPr)_4$ RT", were prepared on top of glass/indium-tin-oxide (ITO) substrates as described in the Methods section. The thickness of $Ti(OiPr)_4$ RT film was measured to be 20 nm using ellipsometry (Supplementary Table 1). Scanning electron microscopy (SEM) images show pin-hole free surface morphology (Supplementary Fig. 1). Hydrolysis and condensation of precursor $Ti(OiPr)_4$ is the key to forming solid thin film[23]. Once the $Ti(OiPr)_4$ precursor solution is spin coated on the ITO slide, the isopropanol solvent evaporates quickly and $Ti(OiPr)_4$ makes contact with moisture in the air. Subsequently, hydrolysis and condensation reactions form Ti-O-Ti linkages[24]. Incomplete condensation will result in an OH group left in the thin film[25], as is the case with our $Ti(OiPr)_4$ RT film (*vide infra*).

We fabricated and tested perovskite solar cells with $Ti(OiPr)_4$ RT films deposited in different relative humidity (RH) to investigate the impact of RH on solar cell efficiency. The device structure is shown in Figures 1a and 1b. On top of the $Ti(OiPr)_4$ RT film, the methylammonium lead iodide ($MAPbI_3$) layer (~300 nm), the spiro-OMeTAD layer (100 nm), and the silver anode layer (60 nm) were deposited as described in the Methods section. The cells with $Ti(OiPr)_4$ RT films fabricated in 40% to 55% RH resulted in the highest efficiency (Supplementary Fig. 2), so all the following $Ti(OiPr)_4$ films were made in 55% RH. Next, to check for the impact of thermal annealing on solar cell efficiency, $Ti(OiPr)_4$ films were annealed immediately after the spin-coating step at various temperatures ranging from room temperature up to 500 ºC. Our results show that the temperature at which the $Ti(OiPr)_4$ thin film is annealed has no significant impact on the solar cell efficiency (Figure 1c). Specifically, the unannealed film (RT) and 500 °C annealed films result in comparable open-circuit voltages (V_{OC}), short-circuit current densities (J_{SC}), fill factors (FF), and efficiencies (η) as shown in Fig. 1d.

Additionally, we examined the impact of thermal annealing temperature on the performance of TiO_2 thin films made from titanium diisopropoxide bis(acetylacetonate) in butanol, from here on referred to as "$Ti(OiPr)_2(AcAc)_2$". This is the most commonly employed TiO_2 precursor solution for high-efficiency perovskite solar cells[26-28] and typically annealed at high temperatures (>450 °C). Our results show that, indeed, when varying the annealing temperature from 25 °C to 500 °C, the solar cell efficiency changes from 11% to 16% (Figure 1c), mostly due to an increase in the J_{SC} (Supplementary Fig. 3). We attribute the starkly different dependence of $Ti(OiPr)_4$ and $Ti(OiPr)_2(AcAc)_2$ performance on the annealing temperature to slower hydrolysis of the acetylacetone groups[29]. $Ti(OiPr)_2(AcAc)_2$ has an octahedral coordination with two isopropoxide and two acetylacetone (AcAc) groups around a central titanium atom. Previous literature has shown that the labile isopropoxide groups can easily hydrolyze compared to AcAc groups[29, 30]. In fact, the AcAc groups have been used to stabilize the solution formulation by suppressing uncontrolled precipitation since hydrolysis of the AcAc groups is significantly more suppressed[31]. Therefore, when $Ti(OiPr)_2(AcAc)_2$ is used as the precursor solution to form the titania ETL, pyrolysis at high temperature is needed rather than just hydrolysis. In contrast, we show in this work that $Ti(OiPr)_4$ can readily form a titania layer at room temperature that performs well in perovskite solar cells.

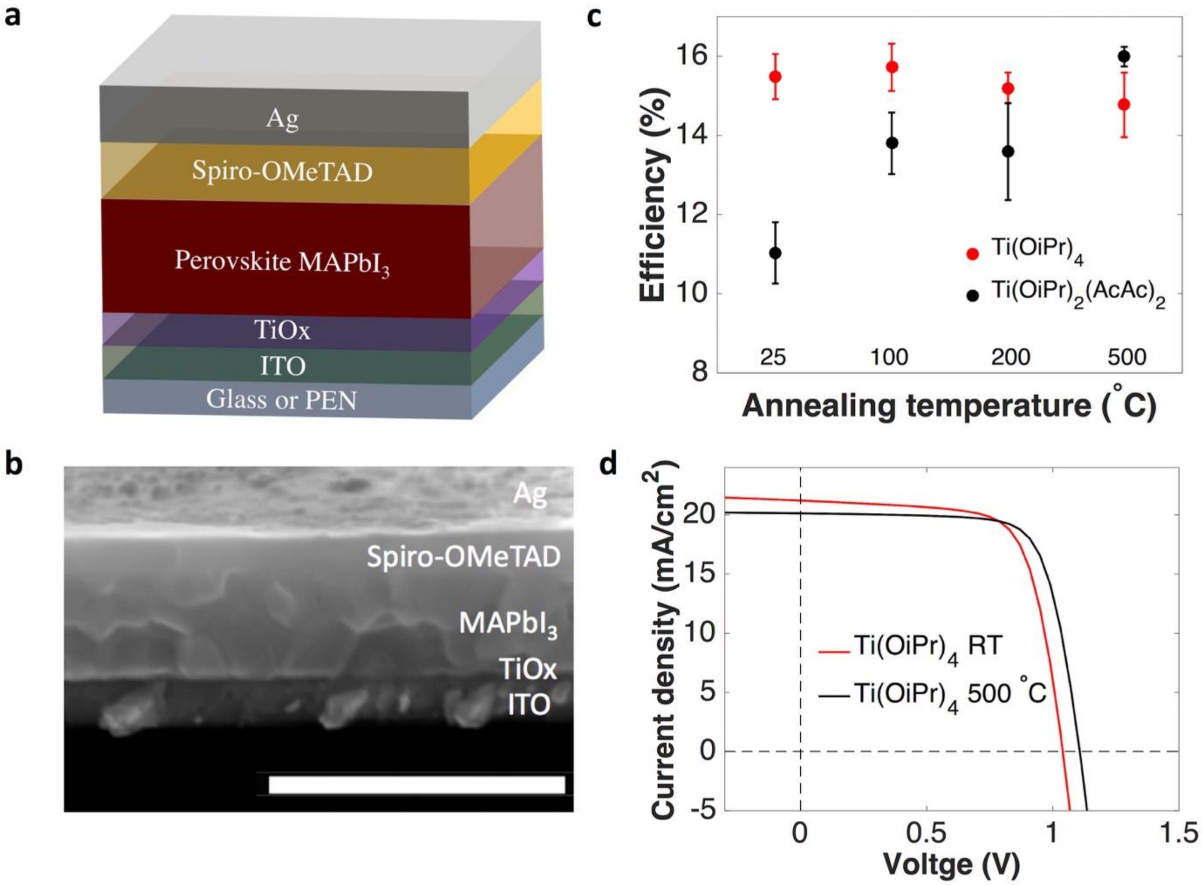

Figure 1: Device structures and their performance. (a) Perovskite solar cell structure. (b) SEM image of device cross-section. Scale bar represents 1 μm. (c) Impact of annealing temperature of ETL on performance of solar cells when two different precursor solutions were used, $Ti(OiPr)_4$ and $Ti(OiPr)_2(AcAc)_2$. (d) J-V curve of champion cell with $Ti(OiPr)_4$ film without annealing and annealed at 500 ºC.

To better understand the nature of the $Ti(OiPr)_4$ RT film, we performed optical, electrical, and X-ray diffraction characterization. The absorbance spectra of the $Ti(OiPr)_4$ RT film and $Ti(OiPr)_2(AcAc)_2$ 500 ºC film were measured using a spectrophotometer equipped with an integrating sphere (Figure 2a). The band gap of $Ti(OiPr)_4$ RT film was determined to be 3.69 eV using a Tauc plot, which matches the band gap of TiO_x reported in the literature[32, 33]. The absorbance onset of precursor $Ti(OiPr)_4$ solution is 3.89 eV which is higher than the deposited $Ti(OiPr)_4$ RT film. The band gap of $Ti(OiPr)_2(AcAc)_2$ 500 °C film was determined to be 3.57 eV, which is slightly lower than the band gap of the $Ti(OiPr)_4$ RT film. Fourier Transform Infrared (FTIR) spectroscopy results are shown in Figure 2b. Both samples show absorption in the region below 1,000 cm^{-1} which corresponds to a vibration peak of Ti–O–Ti bonds[25], suggesting that Ti-O-Ti bonds have formed in both cases.

In higher wavenumber regions, the spectrum from the $Ti(OiPr)_4$ sample shows several peaks that are missing in the spectrum from the $Ti(OiPr)_2(AcAc)_2$ sample. These peaks are associated with O-H groups (2,450 – 3,600 cm^{-1} and 1,600 – 1,700 cm^{-1}), C-O stretching (1,050 –1,180 cm^{-1}), C-H bending (1,350 – 1,410 cm^{-1}), and C-H stretching (2,850 – 3,000 cm^{-1}). These peaks indicate the presence of an OH group as well as organic residues in the $Ti(OiPr)_4$ sample[34]. In a pH neutral condition such as $Ti(OiPr)_4$ in isopropanol (IPA), a significant fraction of the product will form weaker olation bonds, which consist of metal ions bridged through hydroxide, rather than condensation bonds[35]. FTIR spectra indicates the occurrence of a terminal type of OH groups[25], which passivate the dangling bond of the TiO_x film. Therefore, our FTIR results suggest that some of the $Ti(OiPr)_4$ did not completely go through the hydrolysis and condensation steps.

X-ray diffraction (XRD) patterns show no peaks from thin films deposited from $Ti(OiPr)_4$ and annealed below 350 ºC (Figure 2d). If annealed at temperatures above 350 ºC, XRD patterns show peaks that correspond to anatase TiO_2. The transition temperature of ~350 ºC observed in our work is consistent with the transition from the amorphous to the anatase phase of TiO_2[36]. Our Raman spectroscopy results also present a consistent picture that the $Ti(OiPr)_4$ RT sample is completely amorphous since there are no obvious peaks that correspond to crystalline TiO_2 as shown previously in the literature[37] (Figure 2c). In comparison, the $Ti(OiPr)_2(AcAc)_2$ 500 ºC show peaks at 145, 398, 516 and 640 cm^{-1} Raman shift that correspond agreeably to the anatase phase of TiO_2[37].

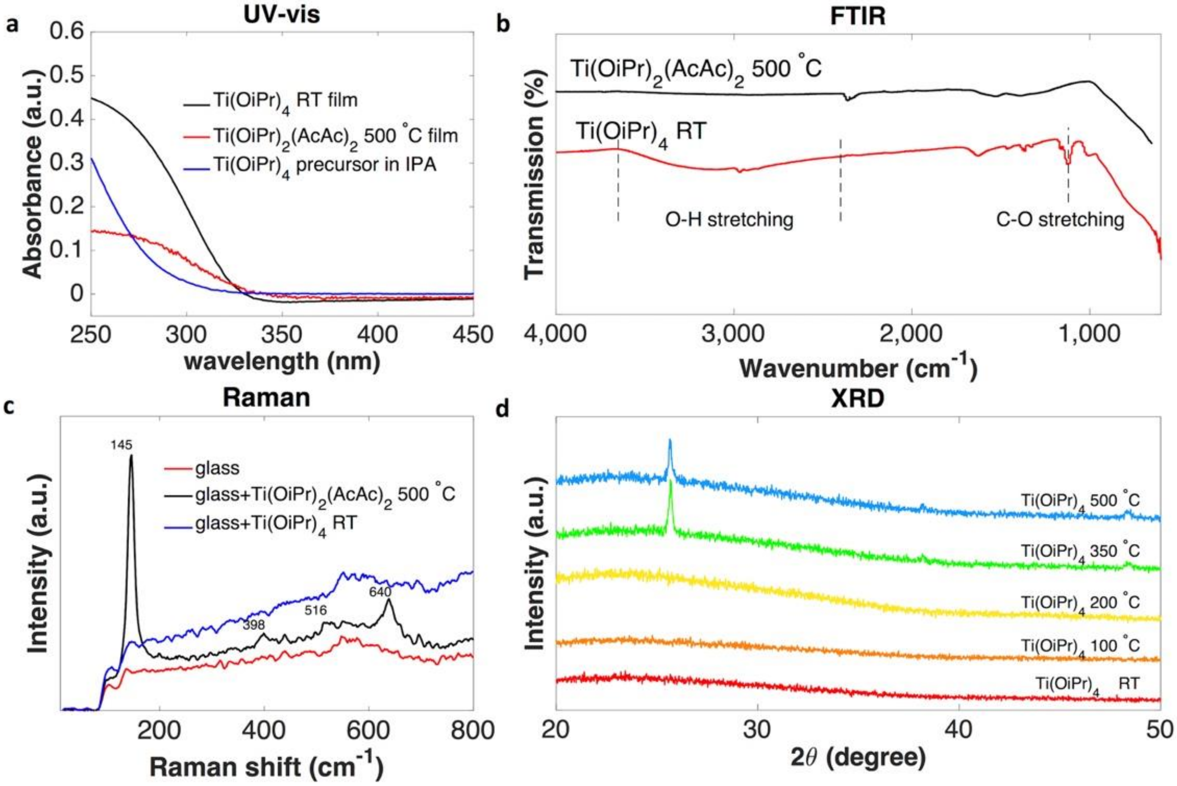

Figure 2: Characterization for $Ti(OiPr)_4$ film. (a) UV-vis absorbance spectra for $Ti(OiPr)_4$ RT film, $Ti(OiPr)_2(AcAc)_2$ 500 ºC film, and $Ti(OiPr)_4$ RT precursor solution. (b) FTIR transmission spectra of $Ti(OiPr)_2(AcAc)_2$ 500 ºC and $Ti(OiPr)_4$ powder. (c) Raman spectra of substrate glass, $Ti(OiPr)_4$ RT film, and $Ti(OiPr)_2(AcAc)_2$ 500 ºC film. (d) XRD of $Ti(OiPr)_4$ film without annealing, annealed at 100 ºC, 200 ºC, 350 ºC, and 500 ºC.

The electrical resistivity was determined using a two-terminal measurement with ITO and thermally evaporated silver as the electrical contacts with TiO_x thin film sandwiched in the middle. The measured resistivities for the TiO_x thin films annealed at different temperatures are shown in Table 1. They are in the range of $60 \sim 150 \times 10^5$ Ω•cm, which lies between that of metals (10^{-6} Ω•cm) and insulators (10^{14} Ω•cm), indicating semiconducting behavior. TiO_2 has a resistivity of 10^8 Ω cm making it electrically insulating, but as the titanium ratio increases relative to the oxide it becomes more like an n-type semiconductor and its resistivity decreases[38]. This indicates that our film is partially suboxidized due to the resistivity being 3 orders of magnitude lower than pure TiO_2. This further indicates that the titanium/oxygen ratio in our films will drastically affect our electrical properties[38]. As the film is annealed at higher temperatures, the observed slight increase in two-terminal resistivity is likely due to the increase in sheet resistance of ITO thin films at temperatures greater than 300 °C. Our TiO_x resistivity measurements are on the same order of magnitude as those obtained from magnetron sputtering at varying substrate temperatures by Su *et al*[39]. Additionally, this high resistivity ensures us that our film is complete and pinhole-free, otherwise short paths would arise and dramatically reduce the measured resistance.

Refractive indices of the $Ti(OiPr)_4$ and $Ti(OiPr)_2(AcAc)_2$ thin films prepared at room temperature, and annealed at 110 °C and 500 °C on ITO coated glass, were measured using ellipsometry (Supplementary Figure 5). The measured spectral refractive indices were obtained in the range of 250 - 750 nm. At 633 nm, our films have a refractive index of 1.75, which is much lower than the value of anatase TiO_2 (2.55)[40], but more close to amorphous TiO_2 (2.03)[40]. This is consistent with our Raman, XRD, and FT-IR results that indicate our film being amorphous TiO_x. The lower refractive indices also indicate that the $Ti(OiPr)_4$ thin films processed at room temperature may be a low density film with organic residues as shown by FT-IR. The refractive index of TiO_2 is known to correlate positively with annealing temperature and titanium oxide density[41, 42].

By employing the room temperature processed TiO_x layer, we have fabricated and tested flexible perovskite solar cells using ITO-coated PEN substrates (Figure 3). The device architecture is shown in Figure 1a. The champion device achieved 14.3% efficiency, with V_{OC} of 1.00 V, J_{SC} of 20.04 mA/cm^2, and FF of 0.71 (Figure 3b). This is close to the record for efficiency of a flexible solar cell based on $MAPbI_3$, 15% to 16%. The highest record efficiency so far by Wang *et al.* of 18% efficiency has been achieved with alloyed perovskites[6]. We emphasize that all of these previous record efficiency results have relied on either vacuum processing (ALD or sputter deposition) or colloidal nanoparticles, whereas our flexible solar cells are based on room temperature and non-vacuum processing with a simple sol-gel precursor. To check for the stability of our flexible solar cells, we monitored the device performance over a time period in nitrogen glovebox storage and found that the device maintained ~90% of its original efficiency after two weeks (Supplementary Figure 6). We have also performed mechanical durability testing by bending the device with a radius of curvature of 5 mm (Supplementary Figure 7). After 300 bending cycles, the device maintained ~85% of its original efficiency. The decrease in efficiency was caused mainly by the reduced J_{SC} and increased series resistance.

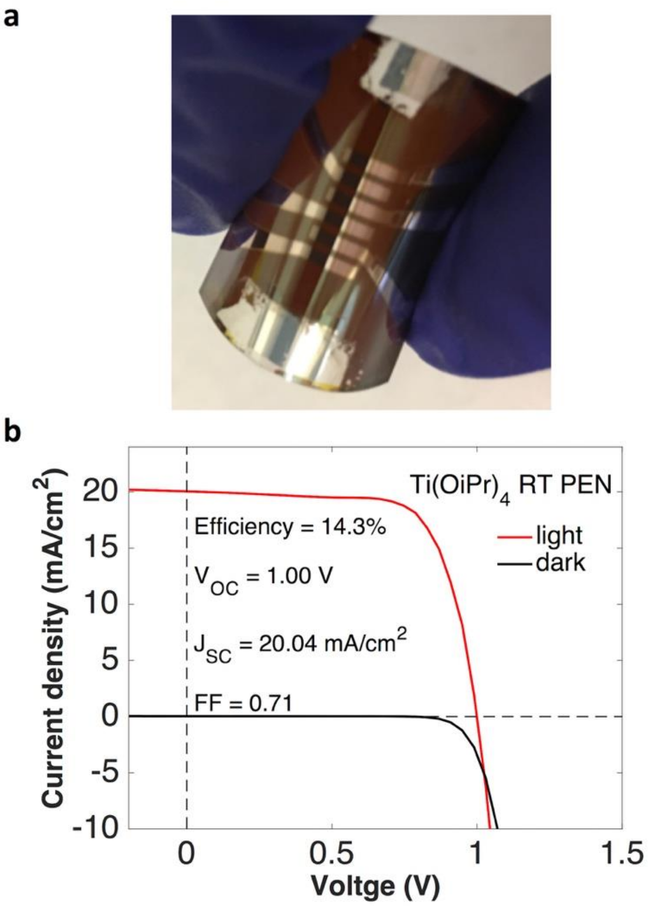

Figure 3: Flexible solar cell. (a) Picture of flexible perovskite solar cell and (b) J–V curves for device fabricated on ITO-covered PEN substrate. Efficiency, VOC (V), JSC (mA/cm−2), and FF are shown in inset.

In summary, we demonstrated room temperature solution processing of amorphous TiO_x thin film with high performance TiO_x ETL in MHP solar cells. We showed that the solar cell efficiency of cells with the TiO_x film annealed at a temperature in the range of room temperature to 500 ºC is similar, suggesting that thermal annealing at high temperature is not necessary to achieve high solar cell performance. Flexible MHP solar cells that employ the room temperature processed TiO_x layer achieved a PCE of 14.3% and show promising stability and mechanical durability. Our work highlights the potential of flexible, lightweight and high efficiency MHP solar cells fabricated all through low-cost, high-throughput, and low thermal budget processing steps.

2.4 Methods

$Ti(OiPr)_4$ RT film

Our TiO_x solution was prepared using a method adapted from Back *et al*[43]. Titanium (IV) isopropoxide ($Ti(OiPr)_4$) was purchased from Sigma-Aldrich and prepared in a 1:50 volume ratio with isopropanol (IPA), which contains 0.02% H_2O. The solution is ready to use immediately without heating. The $Ti(OiPr)_4$ solution was spin-coated onto indium-tin-oxide (ITO) patterned glass at 3,000 rpm for 30 seconds. Compact TiO_2 thin films were fabricated by spin-coating a solution of 146.6 µL $Ti(OiPr)_2(AcAc)_2$ in 2 mL of butanol for 30 s at 4,000 rpm and annealing at 450 ºC for 5 minutes.

Solar cell fabrication

The patterned ITO glass substrate was cleaned sequentially in Hellmanex III detergent, deionized water, and ethanol in an ultrasonic cleaner, rinsed with acetone and IPA, and placed in an ultraviolet ozone plasma cleaner for 5 minutes. The patterned ITO glass and PEN substrates (25.4 mm^2) were purchased from KINTEC Company. Scotch tape was used to cover the end of the ITO contact to protect it from being coated during spin coating. $Ti(OiPr)_4$ RT film was deposited on ITO slides. $MAPbI_3$ was prepared using an adapted inter-diffusion method from Xiao et al[44]. 1M PbI_2 (99.9985%, Alfa Aesar) and anhydrous dimethyl sulfoxide (DMSO, Sigma-Aldrich) were dissolved in anhydrous dimethylformamide (DMF, Sigma-Aldrich) and stirred for 2 hours at 60 ºC. Methylammonium iodide (MAI, Dyesol) was dissolved in anhydrous IPA (Sigma-Aldrich) at 50 mg/mL concentration. Next, the PbI_2 and MAI solutions were spin-coated at 2,000 rpm for 1 minute sequentially and annealed at 110 °C for 12 minutes in a nitrogen-filled glovebox. (2,2′,7,7′-tetrakis N, N-di-p-methoxyphenylamine)-9,9′-spirobi- fluorine (Spiro-OMeTAD, Luminescence Technology Corp.) was dissolved at a 72 mg/mL concentration in anhydrous chlorobenzene purchased from Sigma-Aldrich. It was doped with 28.8 µL of 4-tert-butylpuridine (anhydrous, Sigma-Aldrich) and 17.5 µL of a 520 mg/mL solution of lithium-bis(trifluoromethane)sulfonamide (Li-TFSI, 99.95%, Arldrich) in acetonitrile (anhydrous, Sigma-Aldrich). The Spiro-OMeTAD solution was spin-coated at 4,000 rpm for 30 seconds in a nitrogen-filled glovebox and left to oxidize in dry air overnight. Residue from the scotch tape, the perovskite, and the Spiro-OMeTAD was removed from overtop the ITO contact via scraping with a razor blade. The rear silver (Ag) contact was prepared by thermally evaporating 60 nm of silver at a vacuum of $1x10^{-6}$ mbar. Silver evaporation pellets (99.999%) were purchased from Kurt J. Lesker company. The complete device structure is shown in Figure 1b.

Characterization

Solar cell characterization: The devices were tested using a Keithley source-meter operating at a scan rate of 1 V/s under AM 1.5 illumination from a solar simulator (PV Measurements). Calibration of the light source was done using a reference silicon solar cell and current and height adjustments (PV Measurements). While testing, an optical mask was used to only expose the 0.03 cm^2 active device area.

UV-Vis: UV-Vis spectra of the TiO_x with quartz as substrate was done with a UV/Vis/NIR Lambda 950 S spectrometer from Perkin Elmer. An integrating sphere was used and absorbance of film has been calculated by subtracting transmission and reflection from 1. Band gaps were calculated using the Tauc plot method with indirect band gap power factor.

FT-IR: FT-IR transmission spectra of liquids and powders were collected with a Thermo Scientific Nicolet 6700 FT-IR with MCT/A detector and a SenseIR Technologies DuraScope ATR operating between 650-4,000 cm^{-1}.

Raman spectroscopy: Raman spectra were taken on Renishaw inVia Raman Microscope using an excitation source with a wavelength of 514 nm.

X-ray diffraction: X-ray diffraction spectra were taken with a PANalytical X'Pert Pro MPD XRD with a Cu source operating at 45 kV and 40 mA. All measurements are performed at room temperature.

SEM: Planar and cross-sectional SEM images were captured with an FEI Quanta 650 SEM operating at between 5kV and 15kV accelerating voltage.

Electrical resistivity: Electrical resistivity was measured using a two-terminal method that had ITO and evaporated silver as the electrical contacts at both ends and TiO_x in the middle. A Fluke 289 True RMS Multimeter was used to measure the resistance, and resistivity was calculated from the contact area. Copper tape was used to prevent punch through by the probe. A Jandel Four Point Probe was used to verify sheet resistances of the ITO coated glass substrate.

Ellipsometry: Film thickness and refractive index was calculated using a Horiba Jobin Yvon UVISEL Vis ellipsometer and DeltaPsi2 modeling. Spectroscopic elliposmetry was collected between 250 to 750 nm at a 70° angle of incidence with the modulator and analyzer at 0° and 45°, respectively. A TiO_2 dispersion file was used to model the X-ray spectra of TiO_x thin film. Interfacial regions and surface roughness were accounted for in the modeling.

Table 1 Electrical resistivity of TiO_x thin films prepared from $Ti(OiPr)_4$ solution

Anneal Temp (°C)	Two Terminal Resistivity (10^5 Ω·cm)
25	61.88
110	78.75
300	101.3
500	144.0

2.5 Supplementary Information

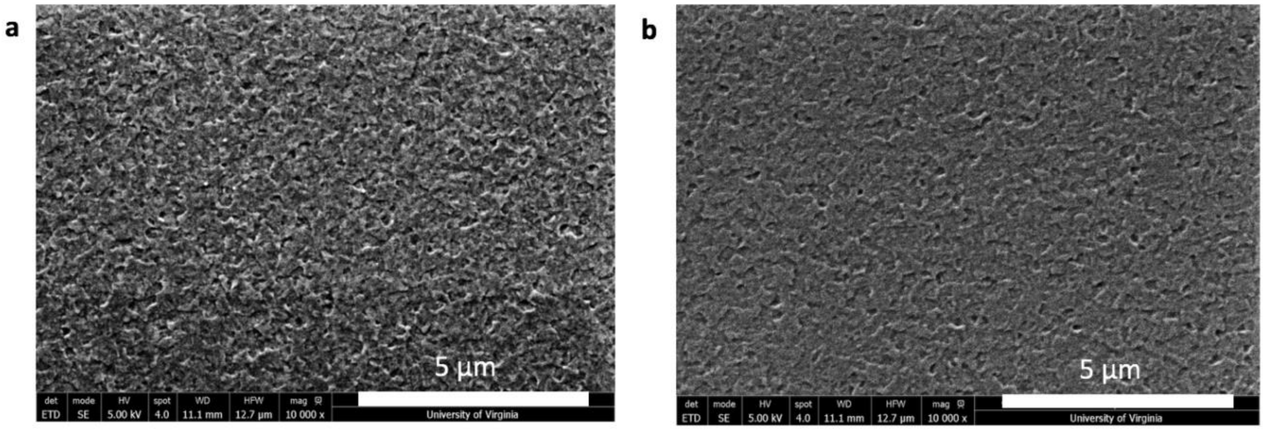

Supplementary Figure 1. Topographical SEM images of the ITO surface and TiO_x film on top of ITO formed by spin-coating $Ti(OiPr)_4$ precursor solution. Images were taken at 5kV accelerating voltage. Scale bar represents 5 μm

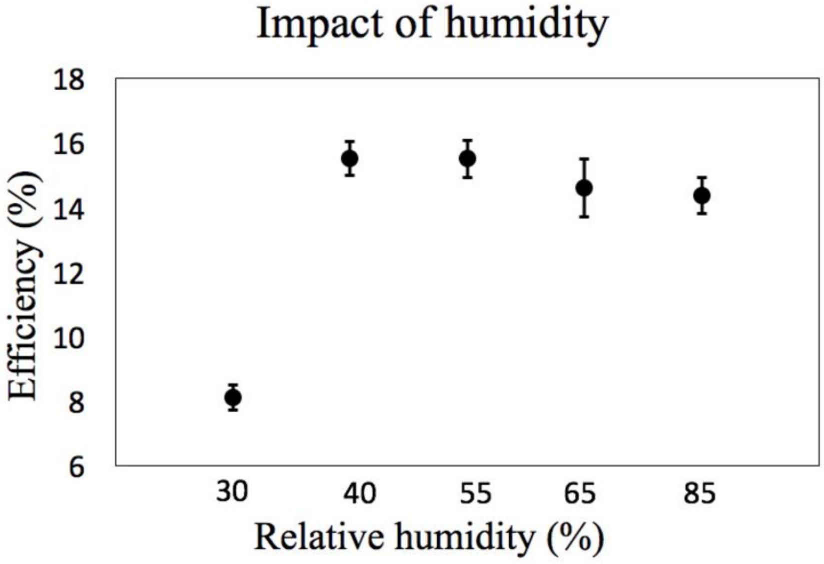

Supplementary Figure 2. Impact of humidity on performance of fabricated solar cells

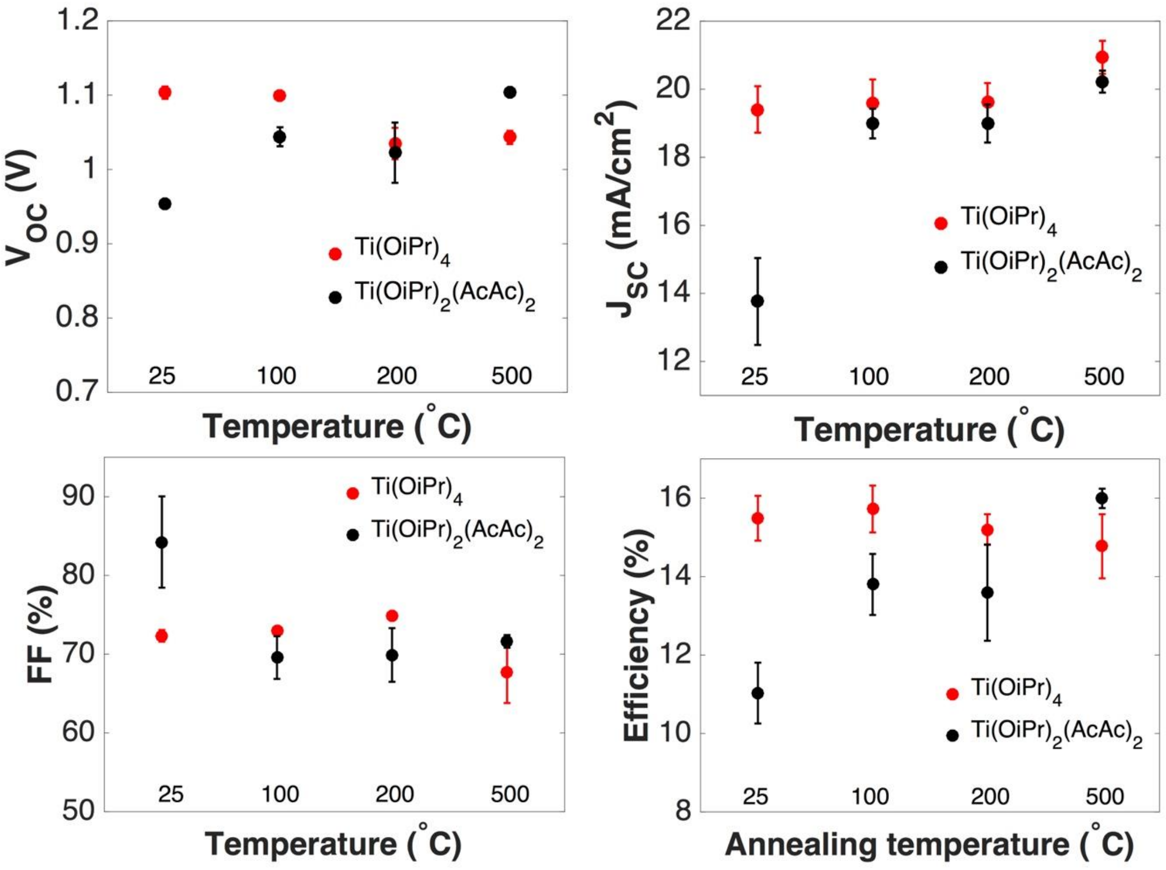

Supplementary Figure 3. Impact of annealing temperature on J_{SC}, V_{OC}, FF, and efficiency of solar cells with ETL made from two different precursor solutions. The temperature range is RT to 500 ºC.

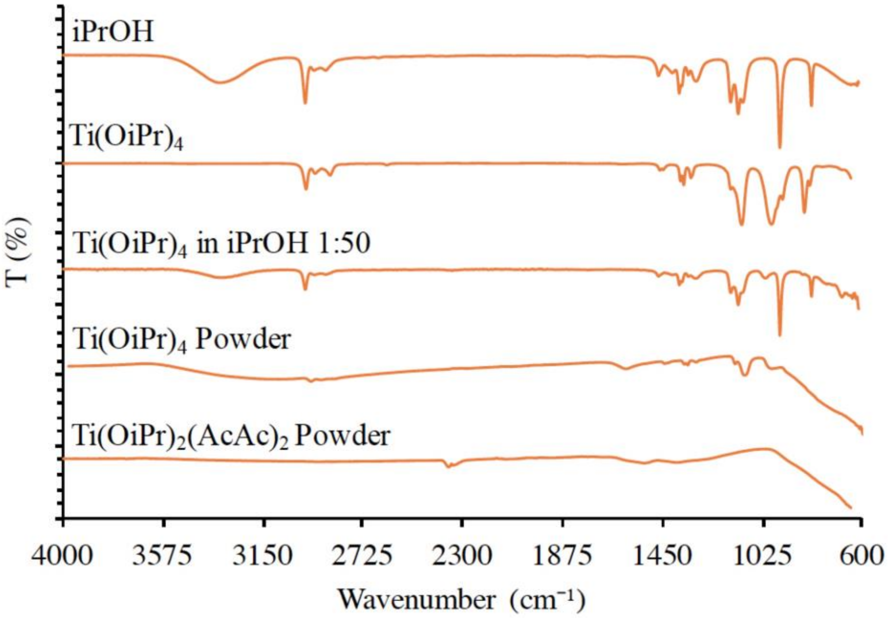

Supplementary Figure 4. FT-IR transmission spectra of IPA, $Ti(OiPr)_4$, diluted $Ti(OiPr)_4$, $Ti(OiPr)_4$ powder, and $Ti(OiPr)_2(AcAc)_2$ powder.

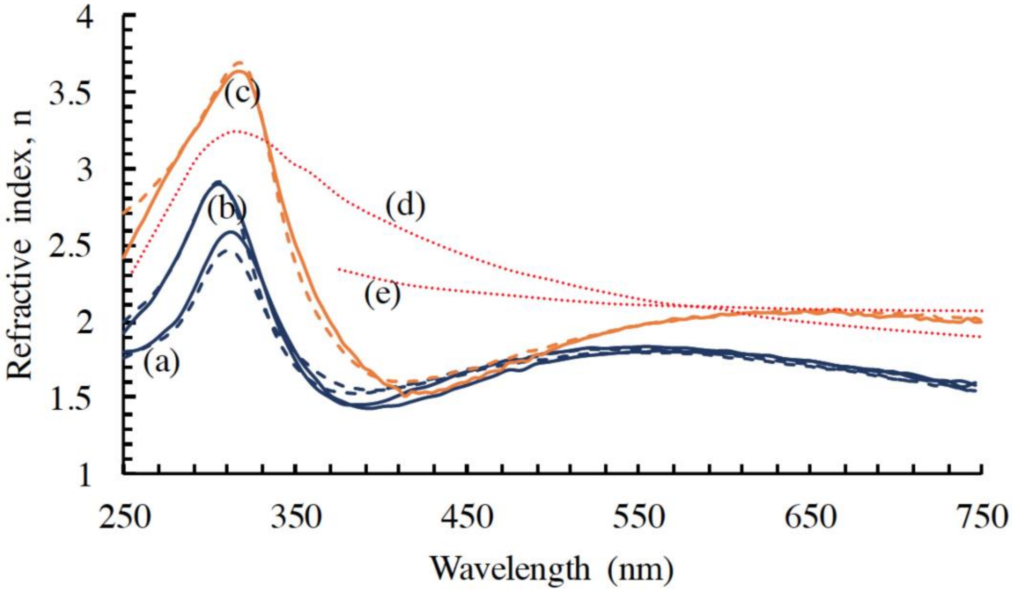

Supplementary Figure 5. Spectral refractive indices for the $Ti(OiPr)_4$ (Blue) and $Ti(OiPr)_2(AcAc)_2$ (Orange) thin films prepared (a) at room temperature, and annealed at (b) 110°C, and (c) 500°C on ITO coated glass. Solid lines indicate data measured from the ellipsometer, while the dashed lines indicate modeled data from DeltaPsi2. Additionally, spectral refractive indices of amorphous (d) and nano crystalline (e) TiO_2 films were obtained from Akimov and Tauson[45] and are overlaid as red dotted lines.

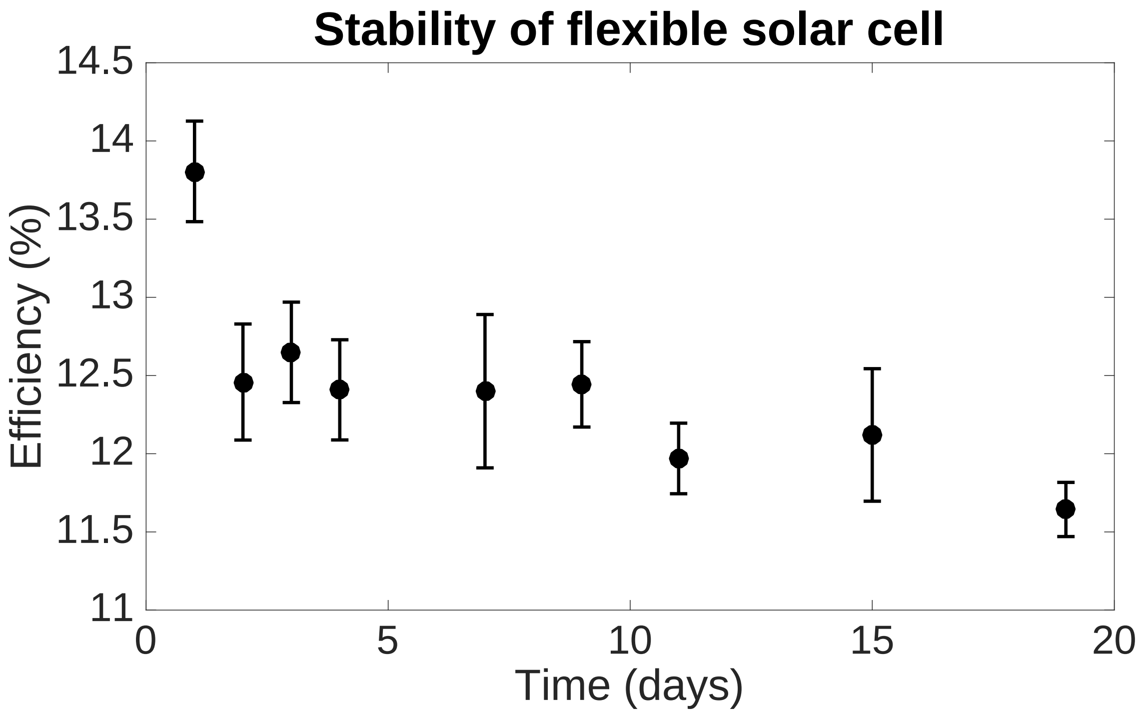

Supplementary Figure 6. Stability of flexible solar cell as a function of storage time in nitrogen glovebox.

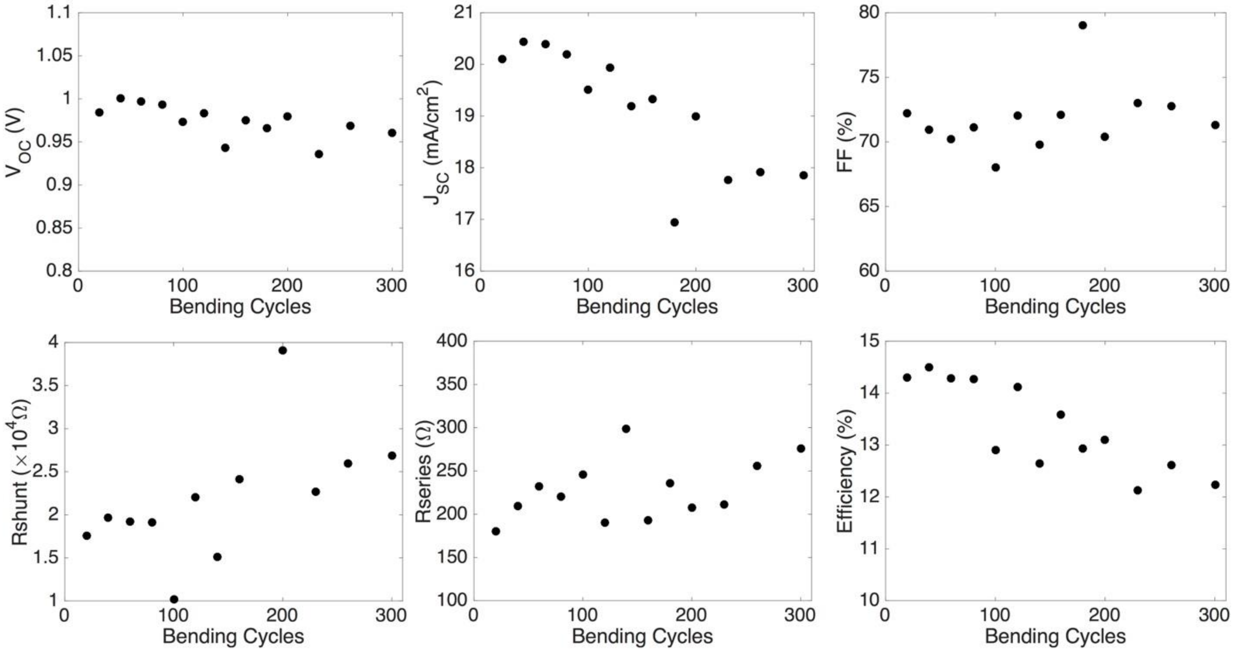

Supplementary Figure 7. Flexible solar cell performance as a function of bending cycles.

Supplementary Table 1. TiO_x film thickness measured using ellipsometry in nanometers

Sample	Interfacial	Film	Roughness	Overall
$Ti(OiPr)_4$ 25 °C	0.000 ± 0.113	20.322 ± 1.233	0.796 ± 0.742	21.118 ± 2.088
$Ti(OiPr)_4$ 110 °C	0.000 ± 0.077	15.509 ± 1.575	2.029 ± 1.069	17.538 ± 2.721
$Ti(OiPr)_2(AcAc)_2$ 500 °C	0.000 ± 0.082	16.636 ± 1.107	1.649 ± 0.769	18.285 ± 1.958

2.6 Reference

1. NREL 2014, [online] Available: http://www.nrel.gov/ncpv/images/efficiency_chart.jpg

2. F. Di Giacomo, A. Fakharuddin, R. Jose, and T.M. Brown, Progress, challenges and perspectives in flexible perovskite solar cells, Energy Environ. Sci. 9 (2016) 3007-3035.

3. S.D. Stranks, G.E. Eperon, G. Grancini, C. Menelaou, M.J.P. Alcocer, and T. Leijtens, Electron-hole diffusion lengths exceeding 1 micrometer in an organometal trihalide perovskite absorber, Science 342 (2013) 341-344.

4. S.S. Mali, C.K. Hong, A.I. Inamdar, H. Im, and S.E. Shim, Efficient planar n-i-p type heterojunction flexible perovskite solar cells with sputtered TiO2 electron transporting layers, Nanoscale 9 (2017) 3095-3104.

5. J.H. Heo, M.H. Lee, H.J. Han, B.R. Patil, J.S. Yu, and S.H. Im, Highly efficient low temperature solution processable planar type CH3NH3PbI3 perovskite flexible solar cells, J. Mater. Chem. A 4 (2016) 1572-1578.

6. C. Wang, D. Zhao, Y. Yu, N. Shrestha, C.R. Grice, W. Liao, A.J. Cimarolib, J. Chen, R.J. Ellingson, X. Zhao, and Y. Yan, Compositional and morphological engineering of mixed cation perovskite films for highly efficient planar and flexible solar cells with reduced hysteresis, Nano Energy 35 (2017) 223-232.

7. K. Wojciechowski, M. Saliba, T. Leijtens, A. Abate, and H.J. Snaith, Sub-150 °C processed meso-superstructured perovskite solar cells with enhanced efficiency, Energy Environ. Sci. 7 (2014) 1142-1147.

8. A. Yella, L.P. Heiniger, P. Gao, M.K. Nazeeruddin, and M. Gratzel, Nanocrystalline rutile electron extraction layer enables low-temperature solution processed perovskite photovoltaics with 13.7% efficiency, Nano Lett. 14 (2014) 2591-6.

9. F. Yang, J. Liu, H.E. Lim, Y. Ishikura, K. Shinokita, Y. Miyauchi, A. Wakamiya, Y. Murata, and K. Matsuda, High Bending Durability of Efficient Flexible Perovskite Solar Cells Using Metal Oxide Electron Transport Layer, J. Phys. Chem. C 122 (2018) 17088-17095.

10. Y. Dkhissi, F. Huang, S. Rubanov, M. Xiao, U. Bach, L. Spiccia, R.A. Caruso, and Y.-B. Cheng, Low temperature processing of flexible planar perovskite solar cells with efficiency over 10%, J. Power Sources 278 (2015) 325-331.

11. S. Das, G. Gu, P.C. Joshi, B. Yang, T. Aytug, C.M. Rouleau, D.B. Geohegan, and K. Xiao, Low thermal budget, photonic-cured compact TiO2 layers for high-efficiency perovskite solar cells, J. Mater. Chem. A 4 (2016) 9685-9690.

12. T. Leijtens, G.E. Eperon, S. Pathak, A. Abate, M.M. Lee, and H.J. Snaith, Overcoming ultraviolet light instability of sensitized TiO2 with meso-superstructured organometal tri-halide perovskite solar cells, Nat. Commun. 4 (2013) 2885-2893.

13. S.S. Shin, W.S. Yang, J.H. Noh, J.H. Suk, N.J. Jeon, J.H. Park, J.S. Kim, W.M. Seong, and S.I. Seok, High-performance flexible perovskite solar cells exploiting Zn2SnO4 prepared in solution below 100 degrees C, Nat. Commun. 6 (2015) 7410.

14. D. Yang, R. Yang, J. Zhang, Z. Yang, S. Liu, and C. Li, High efficiency flexible perovskite solar cells using superior low temperature TiO2, Energy Environ. Sci. 8 (2015) 3208-3214.

15. A. Kogo, S. Iwasaki, M. Ikegami, and T. Miyasaka, An Ultrathin sputtered TiO2 compact layer for mesoporous brookite-based plastic CH3NH3PbI3−xClx solar cells, Chem. Lett. 46 (2017) 530-532.

16. A. Huang, J. Zhu, Y. Zhou, Y. Yu, Y. Liu, S. Yang, S. Ji, L. Lei, and P. Jin, One step spray-coated TiO2 electron-transport layers for decent perovskite solar cells on large and flexible substrates, Nanotechnology 28 (2017) 01LT02.

17. P. Zhou, W. Li, T. Li, T. Bu, X. Liu, J. Li, J. He, R. Chen, K. Li, J. Zhao, and F. Huang, Ultrasonic spray-coating of large-scale TiO2 compact layer for efficient flexible perovskite solar cells, Micromachines 8 (2017) 55.

18. W. Qiu, U.W. Paetzold, R. Gehlhaar, V. Smirnov, H.-G. Boyen, J.G. Tait, B. Conings, W. Zhang, C.B. Nielsen, I. McCulloch, L. Froyen, P. Heremans, and D. Cheyns, An electron beam evaporated TiO2layer for high efficiency planar perovskite solar cells on flexible polyethylene terephthalate substrates, J. Mater. Chem. A 3 (2015) 22824-22829.

19. A.K. Chandiran, A. Yella, M.T. Mayer, P. Gao, M.K. Nazeeruddin, and M. Gratzel, Sub-nanometer conformal TiO2 blocking layer for high efficiency solid-state perovskite absorber solar cells, Adv. Mater. 26 (2014) 4309-12.

20. B.J. Kim, D.H. Kim, Y.-Y. Lee, H.-W. Shin, G.S. Han, J.S. Hong, K. Mahmood, T.K. Ahn, Y.-C. Joo, K.S. Hong, N.-G. Park, S. Lee, and H.S. Jung, Highly efficient and bending durable perovskite solar cells: toward a wearable power source, Energy Environ. Sci. 8 (2015) 916-921.

21. J.-Y. Chen, C.-C. Chueh, Z. Zhu, W.-C. Chen, and A.K.Y. Jen, Low-temperature electrodeposited crystalline SnO 2 as an efficient electron-transporting layer for conventional perovskite solar cells, Sol. Energy Mater. Sol. Cells 164 (2017) 47-55.

22. J. Zhang, E.J. Juárez-Pérez, I. Mora-Seró, B. Viana, and T. Pauporté, Fast and low temperature growth of electron transport layers for efficient perovskite solar cells, J. Mater. Chem. A 3 (2015) 4909-4915.

23. A.E. Danks, S.R. Hall, and Z. Schnepp, The evolution of 'sol–gel' chemistry as a technique for materials synthesis, Mater. Horiz. 3 (2016) 91-112.

24. S.H. Park, A. Roy, S. Beaupré, S. Cho, N. Coates, J.S. Moon, D. Moses, M. Leclerc, K. Lee, and A.J. Heeger, Bulk heterojunction solar cells with internal quantum efficiency approaching 100%, Nat. Photon. 3 (2009) 297-302.

25. M. Nakamura, S. Kato, T. Aoki, L. Sirghi, and Y. Hatanaka, Role of terminal OH groups on the electrical and hydrophilic properties of hydro-oxygenated amorphous TiOx:OH thin films, J. Appl. Phys. 90 (2001) 3391-3395.

26. N.J. Jeon, J.H. Noh, W.S. Yang, Y.C. Kim, S. Ryu, J. Seo, and S.I. Seok, Compositional engineering of perovskite materials for high-performance solar cells, Nature 517 (2015) 476-80.

27. M. Liu, M.B. Johnston, and H.J. Snaith, Efficient planar heterojunction perovskite solar cells by vapour deposition, Nature 501 (2013) 395-8.

28. D. Bi, W. Tress, M.I. Dar, P. Gao, J. Luo, C. Renevier, K. Schenk, A. Abate, J.-D. Decoppet, S.M. Zakeeruddin, M.K. Zakeeruddin, M. Grätzel, and A. Hagfeldt, Efficient luminescent solar cells based on tailored mixed-cation perovskites, Sci. Adv 2 (2016)

29. C. Sanchez, J. Livage, M. Henry, and F. Babonneau, Chemical modification of alkoxide precursors, J. Non-Cryst. Solids 100 (1988) 65-76.

30. K.G. Caulton and L.G. Hubert-Pfalzgraf, Synthesis, structural principles, and reactivity of heterometallic alkoxides, Chem. Rev. 90 (1990) 969-995.

31. E.B. Duoss, M. Twardowski, and J.A. Lewis, Sol-gel inks for direct-write assembly of functional oxides, Advanced Materials 19 (2007) 3485-3489.

32. J.Y. Kim, K. Lee, N.E. Coates, D. Moses, T.-Q. Nguyen, and M. Dante, Efficient tandem polymer solar cells fabricated by all-solution processing, Science 317 (2007) 222-225.

33. M. Nakamuraa, D. Korzecb, T. Aokib, J. Engemanna, and Y. Hatanakaa, Characterization of TiOx film prepared by plasma enhanced chemical vapor deposition using a multi-jet hollow cathode plasma source, Appl. Surf. Sci. 175-176 (2001) 697-702.

34. Y. Wang, Y. Qin, G. Li, Z. Cui, and Z. Zhang, One-step synthesis and optical properties of blue titanium suboxide nanoparticles, J. Cryst. Growth 282 (2005) 402-406.

35. M. Kallala, C. Sanchez, and B. Cabane, Structures of inorganic polymers in sol-gel processes based on titanium oxide, Physical Review E 48 (1993) 3692-3704.

36. O. Khatim, M. Amamra, K. Chhor, A.M.T. Bell, D. Novikov, D. Vrel, and A. Kanaev, Amorphous–anatase phase transition in single immobilized TiO2 nanoparticles, Chem. Phys. Lett. 558 (2013) 53-56.

37. Y. Ji, Growth mechanism and photocatalytic performance of double-walled and bamboo-type TiO2 nanotube arrays, RSC Adv. 4 (2014) 40474-40481.

38. Y. Ju, M. Wang, Y. Wang, S. Wang, and C. Fu, Electrical properties of amorphous titanium oxide thin films for bolometric application, Adv. Cond. Matter Phys. 2013 (2013)

39. H.X. Su, Z.J. Peng, and X.L. Fu, Composition, structure and electrical resistivity of TiOx thin films deposited by RF magnetron sputtering at varied substrate temperatures, Key Eng. Mater. 602-603 (2014) 1039-1042.

40. P. Loper, M. Stuckelberger, B. Niesen, J. Werner, M. Filipic, S.J. Moon, J.H. Yum, M. Topic, S. De Wolf, and C. Ballif, Complex fefractive index spectra of CH3NH3PbI3 perovskite thin films determined by spectroscopic ellipsometry and spectrophotometry, J. Phys. Chem. Lett. 6 (2015) 66-71.

41. C. O. Ayieko, R. J. Musembi, S. M. Waita, B. O. Aduda, and P. K. Jain, Structural and optical characterization of nitrogen-doped TiO2 thin films deposited by spray pyrolysis on fluorine doped tin oxide (FTO) coated glass slides, International Journal of Energy and Engineering 2 (2012) 67-72.

42. D. Mergel, D. Buschendorf, D. Eggert, R. Grammes, and Samset.B, Density and refractive index of TiO2 films prepared by reactive evaporation, Thin Solid Films 371 (2000) 218-224.

43. H. Back, G. Kim, J. Kim, J. Kong, T.K. Kim, H. Kang, H. Kim, J. Lee, S. Lee, and K. Lee, Achieving long-term stable perovskite solar cells via ion neutralization, Energy Environ. Sci. 9 (2016) 1258-1263.

44. Z. Xiao, Q. Dong, C. Bi, Y. Shao, Y. Yuan, and J. Huang, Solvent annealing of perovskite-induced crystal growth for photovoltaic-device efficiency enhancement, Adv. Mater. 26 (2014) 6503-9.

Chapter 3. Low-Temperature Processing of Tin Oxide Electron Transporting Layer for Flexible Perovskite Solar Cells

This chapter was submitted to Solar Energy Materials & Solar Cells

3.1 Abstract

SnO_2 is a promising electron transporting layer for perovskite solar cells due to its high carrier mobility and preferred band edge alignment with perovskite. However, most of the commonly employed processing methods for SnO_2 thin films require high temperatures (above 150 °C). To achieve roll-to-roll manufacturing of flexible perovskite solar cells using inexpensive plastic substrates, low-temperature processes for all device components are required. Here, we demonstrate a facile process for processing SnO_2 thin films at low temperature for flexible perovskite solar cells. Our results show that combining low-temperature thermal annealing and a multi-step ultraviolet oxygen plasma treatment reduces the mid-gap trap states of SnO_2 to a comparable level to that of conventional high-temperature processed thin films, resulting in a device power conversion efficiency of 17.27%.

3.2 Introduction

Metal halide perovskites (MHPs) are among the most promising solar cell materials. In addition to their certified 23.3 %[1] efficiency that is on-par with silicon solar cells, MHP solar cells are expected to be inexpensive because they can be manufactured using simple solution processing.[2, 3] Moreover, MHPs can be processed into thin films at low temperature (below 150 °C), which enables manufacturing of flexible and lightweight solar cells.

TiO_2 is the most commonly used electron transporting layer (ETL)[4-7] for MHP solar cells but its drawbacks include an ultraviolet activated photochemical process that leads to degradation of the MHP[8] and a large hysteresis in MHP solar cells response due to TiO_2's insufficient carrier mobility and shallow conduction band edge energy.[9] Compared to TiO_2, SnO_2 not only has lower processing temperature, but also has a more suitable conduction band edge energy level and higher mobility, resulting in more efficient electron extraction from MHPs.[10] Moreover, SnO_2 based MHP solar cells have shown superior stability due to reduced photochemical reaction with MHPs.[11]

SnO_2 can be fabricated into thin films using a variety of methods such as sol-gel processes, ALD, Spray pyrolysis.[12-16] However, the commonly used solution processing methods typically require thermal annealing above 180 °C,[15] which is incompatible with the flexible low-cost plastic substrates because it induces deformation in polyethylene terephthalate (PET) and polyethylene naphthalene (PEN). Therefore, fabrication of flexible low-cost MHP solar cells with SnO_2 ETLs requires formation of high-quality SnO_2 thin films at lower temperatures (below 150 °C) that are compatible with PET and PEN. To this end, previous reports have studied sol-gel methods (pre-synthesized SnO_2 nanoparticles),[17-20] dual-fuel combustion methods,[21] plasma treatment,[22, 23] atom layer deposition (ALD)[24, 25] and electrodeposition[26] for low-temperature processed SnO_2. The drawbacks of these methods include higher cost (usage of nanoparticles or ALD) or inferior device performance when compared to conventional high-temperature processed SnO_2 based devices.

Here, we demonstrate a facile way of fabricating high-quality SnO_2 thin films as an ETL for flexible MHP solar cells at low temperature. Our ultraviolet photoelectron spectroscopy (UPS) results show that combining low-temperature thermal annealing and UV ozone (UVO_3) treatment results in SnO_2 thin films with low mid-gap state density equivalent to the conventional high temperature SnO_2 thin films. Based on these insights, we demonstrate flexible MHP solar cells with an efficiency of 15.3%.

3.3 Results and discussion

The list of samples examined is the following: (1) SnO_2 thin films processed at high temperature (185 °C) and treated with UVO_3 will be referred to as “185 °C control sample” from this point on, (2) SnO_2 thin films treated with UVO_3 multiple times during 140 °C annealing as “140 °C multi-step UVO_3 sample”, and (3) SnO_2 thin films annealed at 140 °C and then treated with UVO_3 as “140 °C post UVO_3 sample”. The detailed procedure for sample preparation is described in the experimental section of the Supporting Information. Absorbance spectroscopy results (Fig. S1) show that all the samples have similar spectra with optical band gap of 4 eV, which is consistent with previous reports.[27-29] Therefore, these results suggest that, for all of the three different processing methods, hydrolysis reaction of $SnCl_2 \cdot 2H_2O$ is induced resulting in the formation of SnO_2.

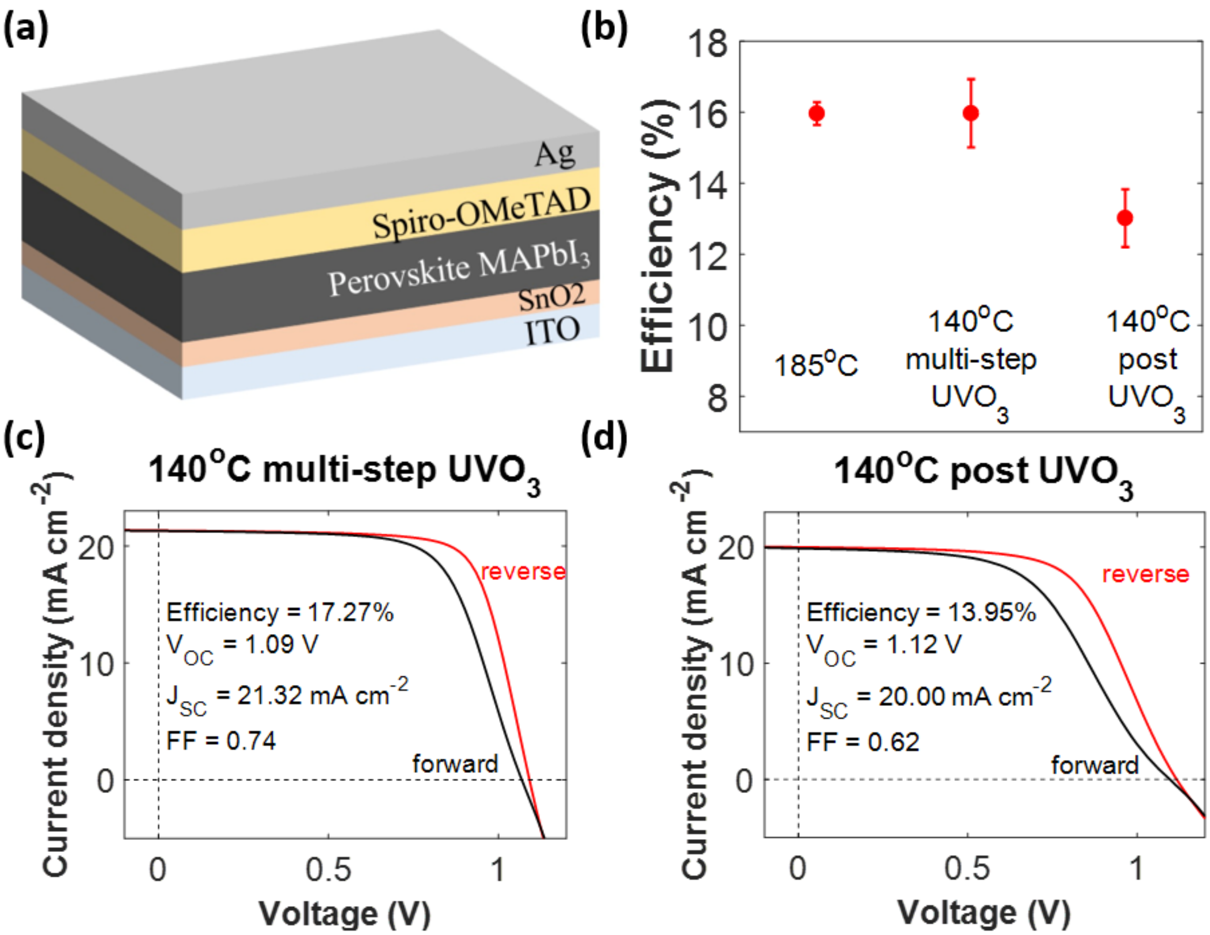

Fig. 1 (a) Solar cell structure. (b) Efficiency results of solar cell with 185 °C SnO_2, 140 °C multi-step UVO_3 SnO_2 and 140 °C post UVO_3 SnO_2 as ETL. (c) J-V curve of 140 °C multi-step UVO_3 SnO_2. (d) J-V curve of 140 °C post UVO_3 SnO_2.

The three different kinds of SnO_2 thin films were employed as ETL in perovskite solar cells to study their impact on solar cell performance, as shown in Figure 1a. The SnO_2 thin films were deposited on indium tin oxide (ITO) substrates. Subsequently, a $(FAPbI_3)_{0.85}(MAPbBr_3)_{0.15}$ alloyed perovskite layer was deposited on top of SnO_2 layer using a solvent engineering method described in the Supporting Information. A 2,2',7,7'-Tetrakis(N,N-di-p-methoxyphenylamino)-

9,9'-spirobifluorene (Spiro-OMeTAD) hole transporting layer (HTL) and a 60 nm of silver anode were deposited to fully form the device. Figure 1b shows power conversion efficiency based on statistics from 12 devices under Air Mass 1.5 irradiation. Solar cells with 140 °C multi-step UVO_3 SnO_2 have as high efficiency as the solar cells with 185 °C SnO_2, while the solar cells with 140 °C post UVO_3 SnO_2 thin film result in significantly lower efficiency. The champion solar cell with 140 °C multi-step SnO_2 achieved efficiency of 17.27 %, with an open-circuit voltage (V_{OC}) of 1.09 V, a short-circuit current density (J_{SC}) of 21.32 mA cm^{-2}, and a fill factor (FF) of 0.74. A comparison of J-V curves from devices with the 140 °C multi-step UVO_3 SnO_2 (Figure 1c) and the 140 °C post UVO_3 SnO_2 (Figure 1d) shows that they have similar V_{OC} and J_{SC}, but the 140 °C multi-step UVO_3 SnO_2 results in higher efficiency mostly due to lower series resistance (Fig. S2) and higher FF. The higher series resistance in the devices with the 140 °C post UVO_3 SnO_2 results in a significant distortion of the J-V curve of solar cells into an S-shape curve (Figure 1d). This can be attributed to unbalanced electron and hole transportation.[30]

Scanning electron microscopy (SEM) images (Figure S3) of the perovskite thin films on top of these different SnO_2 thin films show that there are no significant morphological differences in perovskite thin films. The similar perovskite morphology combined with the same HTL material, Spiro-OMeTAD which is a commonly used HTL material in the state-of-art perovskite devices,[31, 32] suggests that the interface between the HTL and perovskite is not likely to be the source of the substantially more significant S-shape J-V curve for the solar cells with 140 °C post UVO_3 SnO_2.

To better understand this, the differences in the electronic quality of SnO_2 thin films also need to be considered. To this end, the energy levels and valence band spectra of the SnO_2 thin films were studied with ultraviolet photoemission spectroscopy (UPS). The results are shown in Figure 2. The highest intensity feature in each UPS spectra is attributed to O-2p states which make up the valence band maximum (VBM) of SnO_2.[33] The linear edge of this feature is extrapolated to the noise level to determine the VBM energy level relative to the Fermi energy.[34, 35] UPS measures the electron counts with certain kinetics energy, so the shoulder on the low binding energy side of the VBM in each spectrum is attributed to defect states within the band gap, which are likely comprised of hybridized Sn-5s and O-2p states in sub-stoichiometric SnO_2 [33, 36] The 185 °C SnO_2 sample and 140 °C multi-step UVO_3 SnO_2 sample appear to show negligible differences in the position of the VBM or magnitude of defect states. In contrast, the 140 °C post UVO_3 SnO_2 sample can be characterized by having a VBM closer to the Fermi energy (less n-type) with a significantly higher degree of defect states in the bandgap. These takeaways are most easily seen in Fig 2d, where each UPS spectra was normalized to the intensity of the most prominent feature (located at about 5 eV BE). These results suggest that the larger mid-gap trap density of 140 °C post UVO_3 SnO_2 is a major contributing factor to less efficient charge transport, higher resistance and lower fill factor compared to the 185 °C SnO_2 or 140 °C multi-step UVO_3 SnO_2. The implication of these results is that highly oxidizing conditions of UVO_3 processing is helpful to reduce the mid-gap trap states. If the UVO_3 treatment is applied during the sol-gel reaction, SnO_2 thin films with high electronic quality at low temperature (< 150 °C) can be formed that are on-par with their high temperature processed counterparts.

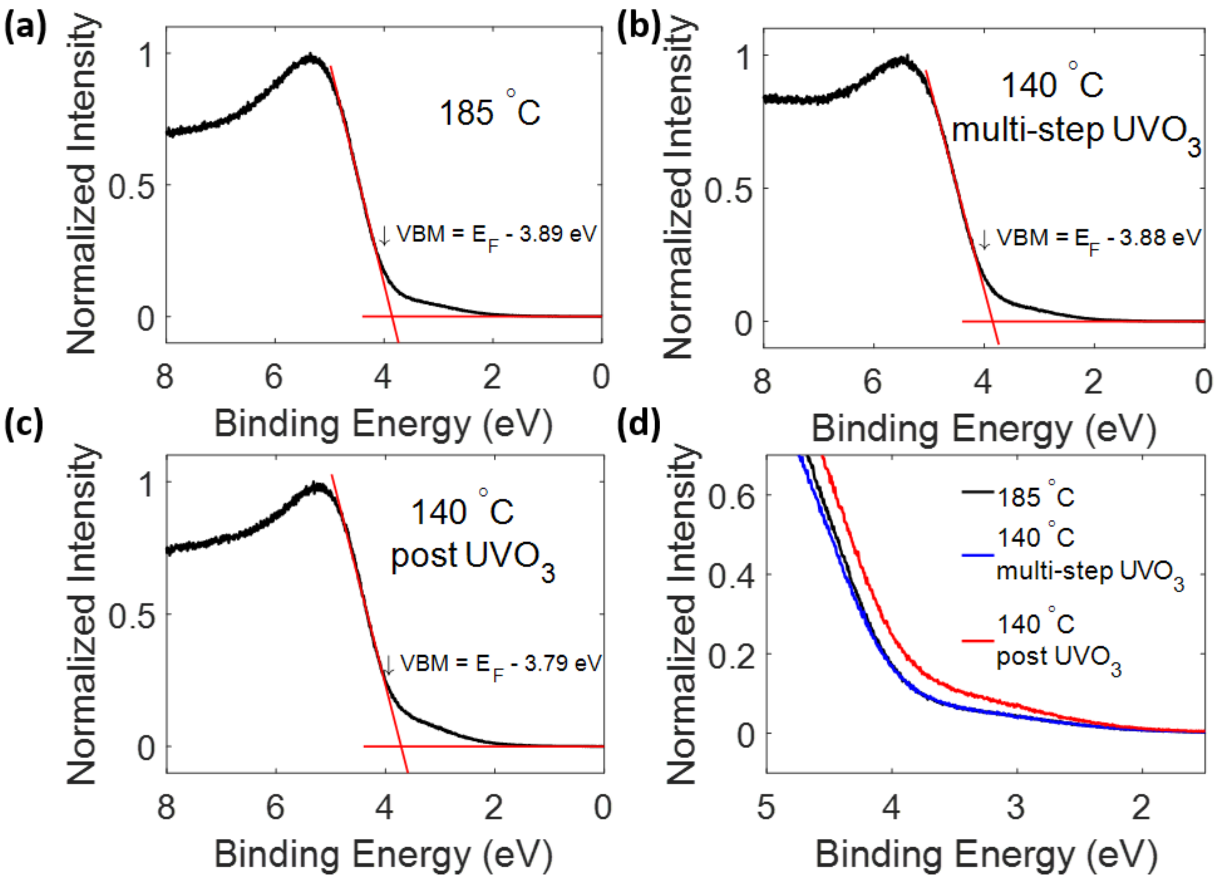

Fig. 2 UPS of 185 °C SnO_2 (a), 140 °C multi-step UVO_3 SnO_2 (b), 140 °C post UVO_3 SnO_2 (c) and comparison of them (d). Helium I was used as the UV photon source for all of them.

With better understanding and control over obtaining high electronic quality SnO_2 thin films at low temperature, we fabricated and tested flexible perovskite solar cells. The 140 °C multi-step UVO_3 SnO_2 was employed as an ETL on ITO-coated PEN substrates. All other layers were deposited in the same manner as the rigid solar cell devices described above. A picture of a flexible perovskite solar cell with the 140 °C multi-step UVO_3 SnO_2 ETL is shown in Figure 3a. The champion cell achieved an efficiency of 15.3 % with a V_{oc} of 1.09 V, J_{sc} of 21.44 mA cm^{-2}, and FF of 0.66. The stability test shows that the device keeps 80 % of original efficiency after two weeks under N_2 storage. To examine mechanical robustness, a bending test was performed with the radius of curvature of 5 mm. After 1000 bending circles, the cell maintained the 85 % of its original efficiency. While the J_{sc} and V_{oc} were barely changed during the bending cycles, increased series resistance was responsible for the reduction in efficiency, which is consistent with bending test results reported previously.[37]

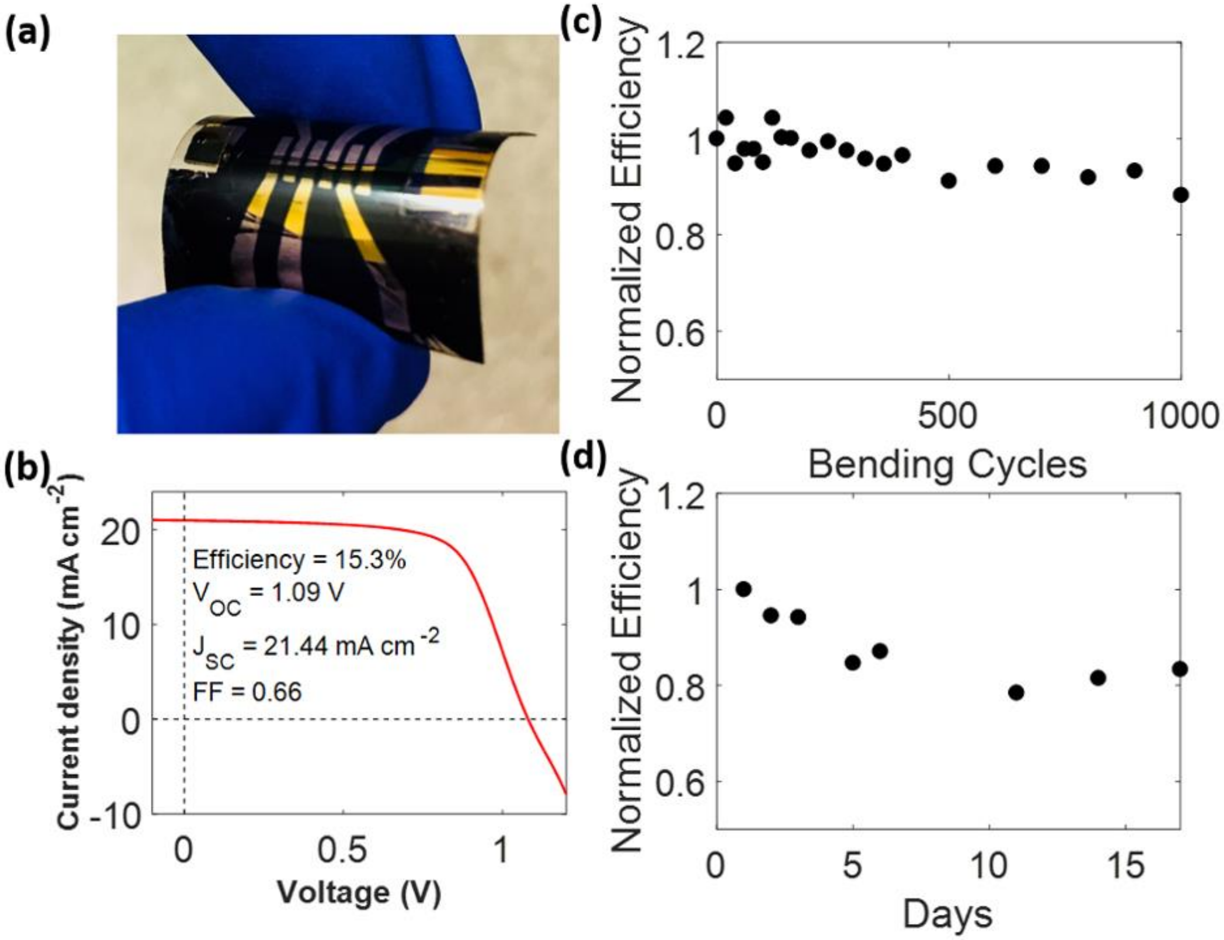

Fig 3 (a) Picture of a flexible solar cell with a 140 °C multi-step UVO_3 SnO_2 ETL. (b) J-V curve and parameters of flexible solar cells with a 140 °C multi-step UVO_3 SnO_2 as ETL. (c) Bending test of flexible solar cells with 5 mm radius of curvature. (d) Stability test of flexible solar cells.

In summary, we demonstrate a facile method to deposit high-quality SnO_2 thin films at low temperatures. Our results show that multi-step UVO_3 treatment throughout the thermal annealing and sol-gel reaction is advantageous. We showed that perovskite solar cells with SnO_2 thin film ETLs deposited at low temperature can achieve efficiencies as high as the solar cells with high temperature SnO_2 ETLs. Rigid solar cells with 17.3% efficiency and flexible solar cells with 15.3% were achieved with promising long-term stability and mechanical robustness.

3.4 Methods

SnO_2 thin film depositions methods

A solution of 0.1 M $SnCl_2 \cdot 2H_2O$ in ethanol was prepared in a purge box with relative humidity of 25%. The solution was filtered through a 0.45 µm PTFE filter and was stored in the purge box at room temperature for 1.5 hours. To form SnO_2 thin films, the solution was spin-coated at 2000 rpm for 40 s on indium-tin-oxide (ITO) patterned glass, which will be referred to as 'pre-deposited SnO_2' from this point on. The "pre-deposited SnO_2" was then processed at different conditions described below.

185 °C SnO_2: High temperature SnO_2 thin film was prepared by annealing the pre-deposited SnO_2 at 185 °C for one hour and treated with ultraviolet ozone plasma (UVO_3) for 10 minutes. This sample will be referred as '185 °C SnO_2'.

140 °C multi-step UVO_3 SnO_2: The pre-deposited SnO_2 was thermally annealed at 140 °C for half of an hour, treated with UVO_3 for 10 minutes, then thermally annealed at 140 °C for another half of an hour, and finally treated with 10 minutes of additional UVO_3.

140 °C post UVO_3 SnO_2: The pre-deposited SnO_2 was thermally annealed at 140 °C for one hour and treated with UVO_3 for 10 minutes.

Solar cell fabrication: The patterned indium tin oxide (ITO) glass and polyethylene naphthalate (PEN) substrates were purchased from KINTEC Company. The patterned ITO substrates were cleaned by sonicating sequentially in Hellmanex III detergent, deionized water, and ethanol in an ultrasonic cleaner, rinsed with acetone and isopropanol (without acetone for PEN slides), and treated by ultraviolet ozone plasma for 10 minutes. Different SnO_2 electron transporting layers were deposited on top of the ITO layers based on the procedures described above. A perovskite precursor solution of $(FAPbI_3)_{0.85}(MAPbBr_3)_{0.15}$ with a 1.8 M concentration was prepared by dissolving 705.34 mg of PbI_2 (Sigma), 99.09 mg of $PbBr_2$ (TCI), 30.23 mg of CH_3NH_3Br (MABr, Dyesol) and 263.11 mg of formadinium iodide (FAI, Dyesol) in 800 μL of anhydrous dimethylformamide (DMF, Sigma) and 200 μL of anhydrous dimethyl sulfoxide (DMSO, Sigma). The solution was stirred on a hotplate at 60 °C for several hours until all solids were dissolved, then was filtered with 0.45 μL PTFE filter. The filtered solution was coated on the SnO_2 layers using a consecutive two-step spin-coating process at 1,000 and 6,000 r.p.m for 10 and 30 s. Chlorobenzene was dropped onto the thin film after the second step as the anti-solvent for perovskite formation. The thin film was annealed at 150 °C for 15 min. 2,2',7,7'-Tetrakis(N,N-di-p-methoxyphenylamino)-9,9'-spirobifluorene (Spiro-OMeTAD, Luminescence Technology Corp.) was dissolved in anhydrous chlorobenzene (Sigma-Aldrich) at a concentration of 72 mg mL^{-1}. A 28.8 μL of anhydrous 4-tert-butylpuridine (Sigma-Aldrich) and a 17.5 μL of a 520 mg mL^{-1} solution of bis(trifluoromethane)sulfonamide (Li-TFSI, 99.95%, Aldrich) in acetonitrile (anhydrous, Sigma-Aldrich) were added to the solution as dopants. The Spiro-OMeTAD thin film was spin-coated at 4,000 rpm for 30 seconds in a nitrogen-filled glovebox and left to oxidize in dry air overnight. Silver (99.999%, Kurt J. Lesker) was thermally evaporated on rigid devices, and gold (99.999%, Kurt J. Lesker) was evaporated on flexible devices.

Characterization:

Ultraviolet photoemission spectroscopy (UPS): UPS spectra were acquired using He I emission as a photon source (hν = 21.22 eV) and a pass energy of 2 eV. Full details of the experimental setup are described elsewhere.[38] The Fermi energy was calibrated to a 0 eV binding energy (BE) using the Fermi edge of a Ag calibration sample which was sputter cleaned in-situ.

Solar cell characterization: A Keithley source-meter operating at a scan rate of 1 V s^{-1} under Air Mass 1.5 illumination from a solar simulator (PV Measurements) was used to test solar cells. Calibration of the light source was done using a reference silicon solar cell. An optical mask was used to ensure the device area was 0.03 cm^2.

UV-Vis: A UV/Vis/NIR Lambda 950 S spectrometer from Perkin Elmer with an integrating sphere was used to measure absorbance spectra of the SnO_2 thin films.

SEM: Planar and cross-sectional SEM images were captured with an FEI Quanta 650 SEM operating at between 5 kV and 15 kV accelerating voltage.

3.5 Supplementary information

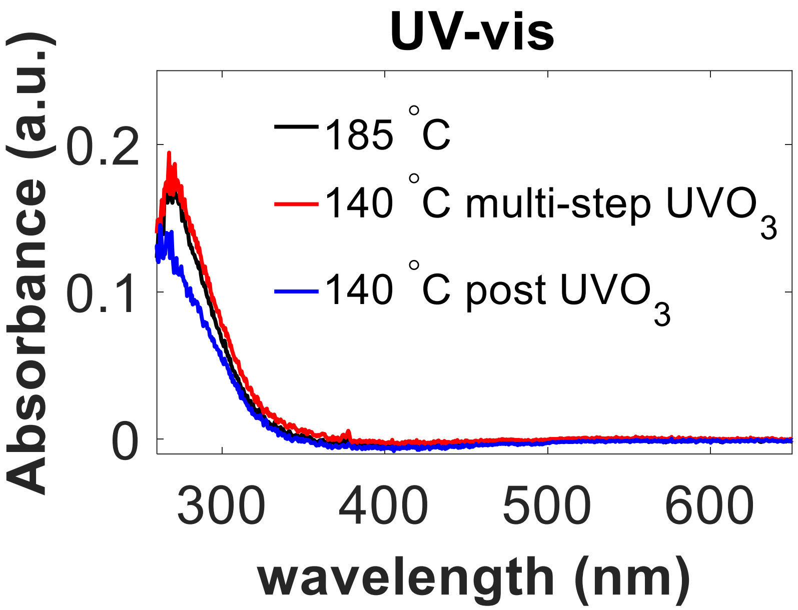

Fig. S1 Absorbance spectra of 185 °C SnO_2, 140 °C multi-step UVO_3 SnO_2 and 140 °C post UVO_3 SnO_2.

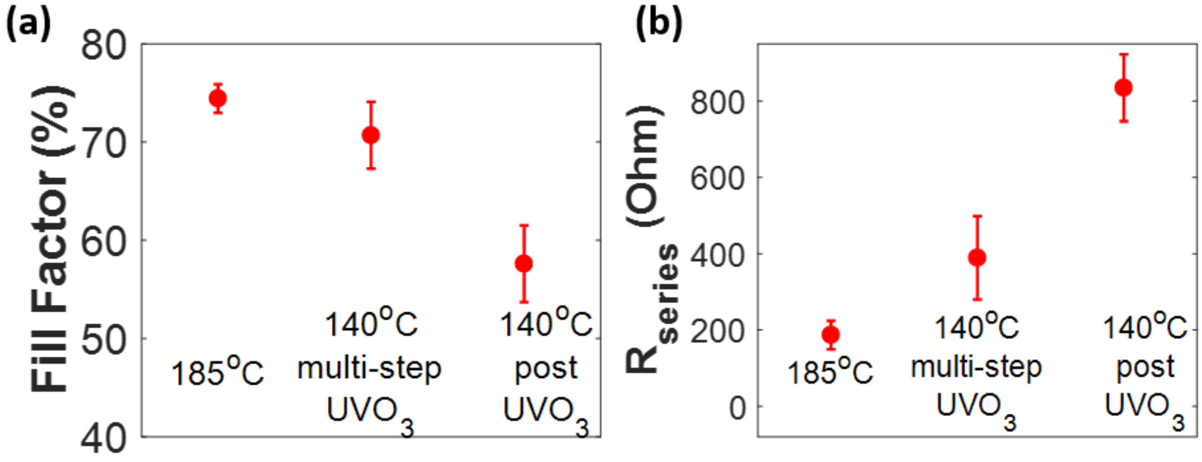

Fig. S2 (a) Fill factor of solar cells with 185 °C SnO_2, 140 °C multi-step UVO_3 SnO_2 and 140 ° post UVO_3 SnO_2 as ETLs. (b) Series resistance of solar cells with 185 °C SnO_2, 140 °C multi-step UVO_3 SnO_2 and 140 °C post UVO_3 SnO_2 as ETLs.

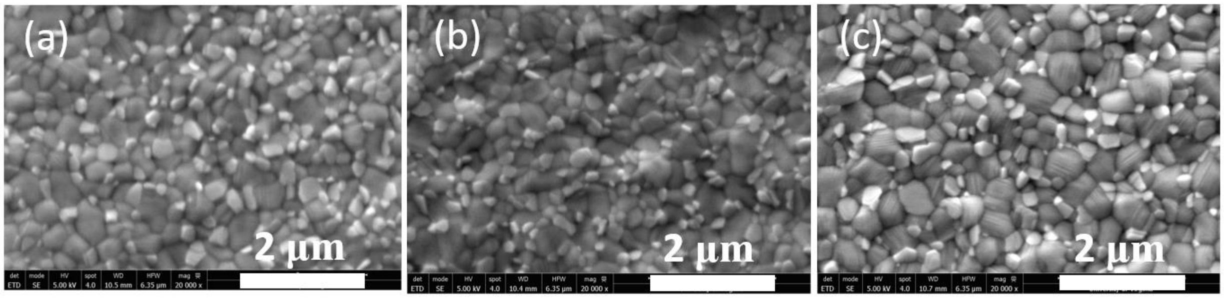

Fig. S3 SEM images of perovskite thin films on top of (a) 185 °C SnO_2, (b) 140 °C multi-step UVO_3 SnO_2 and (c) 140 °C post UVO_3 SnO_2.

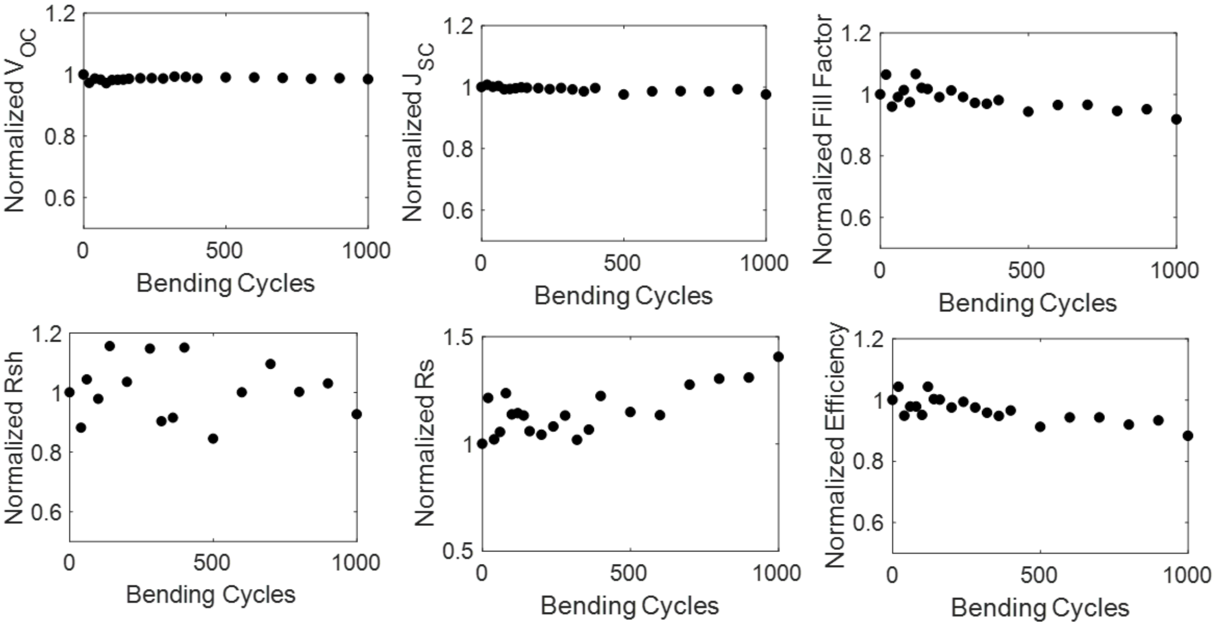

Fig. S4 Bending test results from mechanical bending tests of 140 °C multi-step UVO_3 SnO_2 flexible solar cells.

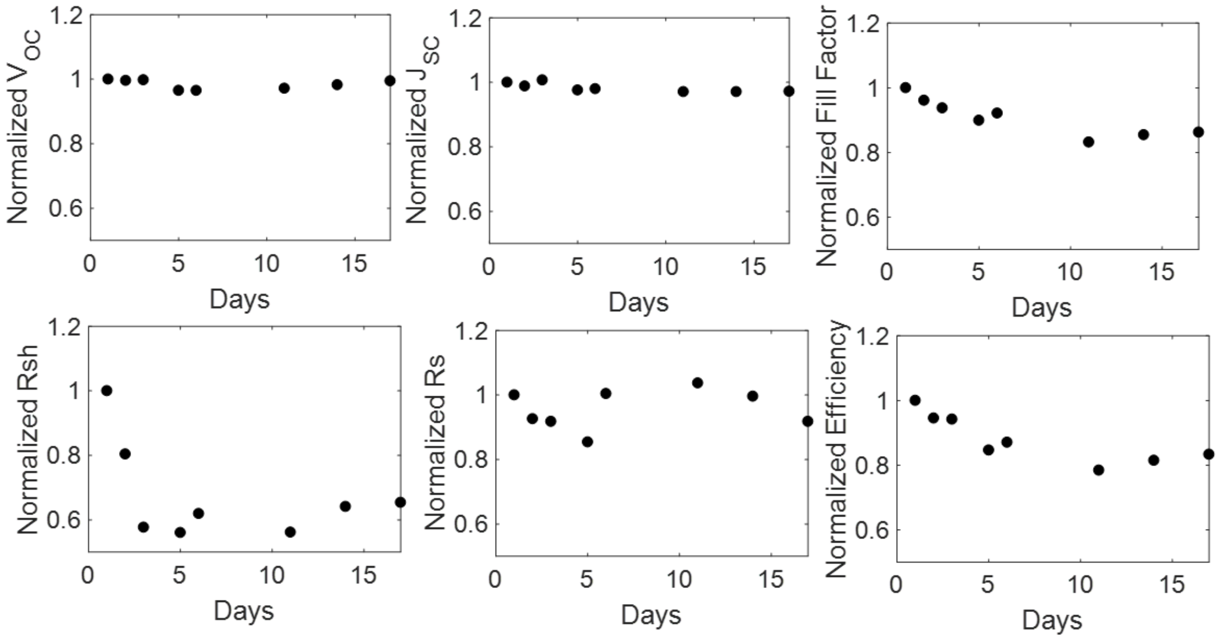

Fig. S5 Stability of 140 °C multi-step UVO$_3$ SnO$_2$ flexible solar cells.

3.6 Reference

1. N.R.C.R.E.C. https://www.nrel.gov/pv/assets/images/efficiency-chart-20180716.jpg,
2. B.J. Foley, J. Girard, B.A. Sorenson, A.Z. Chen, J. Scott Niezgoda, M.R. Alpert, A.F. Harper, D.-M. Smilgies, P. Clancy, W.A. Saidi, and J.J. Choi, Controlling nucleation, growth, and orientation of metal halide perovskite thin films with rationally selected additives, J. Mater. Chem. A 5 (2017) 113-123.
3. B.J. Foley, S. Cuthriell, S. Yazdi, A.Z. Chen, S.M. Guthrie, X. Deng, G. Giri, S.-H. Lee, K. Xiao, B. Doughty, Y.-Z. Ma, and J.J. Choi, Impact of Crystallographic Orientation Disorders on Electronic Heterogeneities in Metal Halide Perovskite Thin Films, Nano Lett. 18 (2018) 6271-6278.

4. X. Deng, G.C. Wilkes, A.Z. Chen, N.S. Prasad, M.C. Gupta, and J.J. Choi, Room-Temperature Processing of TiOx Electron Transporting Layer for Perovskite Solar Cells, J. Phys. Chem. Lett 8 (2017) 3206-3210.
5. I. Jeong, Y.H. Park, S. Bae, M. Park, H. Jeong, P. Lee, and M.J. Ko, Solution-Processed Ultrathin TiO2 Compact Layer Hybridized with Mesoporous TiO2 for High-Performance Perovskite Solar Cells, ACS Appl. Mater. Interfaces 9 (2017) 36865-36874.
6. C. Zhang, Y. Luo, X. Chen, W. Ou-Yang, Y. Chen, Z. Sun, and S. Huang, Influence of different TiO2 blocking films on the photovoltaic performance of perovskite solar cells, Appl. Surf. Sci. 388 (2016) 82-88.
7. G.C. Wilkes, X. Deng, J.J. Choi, and M.C. Gupta, Laser Annealing of TiO2 Electron-Transporting Layer in Perovskite Solar Cells, ACS Appl. Mater. Interfaces 10 (2018) 41312-41317.
8. T. Leijtens, G.E. Eperon, S. Pathak, A. Abate, M.M. Lee, and H.J. Snaith, Overcoming ultraviolet light instability of sensitized TiO2 with meso-superstructured organometal tri-halide perovskite solar cells, Nat. Commun. 4 (2013) 2885-2893.
9. A.-N. Cho and N.-G. Park, Impact of Interfacial Layers in Perovskite Solar Cells, ChemSusChem 10 (2017) 3687-3704.
10. Q. Jiang, L. Zhang, H. Wang, X. Yang, J. Meng, H. Liu, Z. Yin, J. Wu, X. Zhang, and J. You, Enhanced electron extraction using SnO2 for high-efficiency planar-structure HC(NH2)2PbI3-based perovskite solar cells, Nat. Energy. 2 (2016) 16177-16184.
11. B. Roose, J.-P.C. Baena, K.C. Gödel, M. Graetzel, A. Hagfeldt, U. Steiner, and A. Abate, Mesoporous SnO2 electron selective contact enables UV-stable perovskite solar cells, Nano Energy 30 (2016) 517-522.

12. S.S. Mali, J.V. Patil, H. Kim, and C.K. Hong, Synthesis of SnO2 nanofibers and nanobelts electron transporting layer for efficient perovskite solar cells, Nanoscale 10 (2018) 8275-8284.

13. E. Halvani Anaraki, A. Kermanpur, M.T. Mayer, L. Steier, T. Ahmed, S.-H. Turren-Cruz, J. Seo, J. Luo, S.M. Zakeeruddin, W.R. Tress, T. Edvinsson, M. Grätzel, A. Hagfeldt, and J.-P. Correa-Baena, Low-Temperature Nb-Doped SnO2 Electron-Selective Contact Yields over 20% Efficiency in Planar Perovskite Solar Cells, ACS Energy Lett. 3 (2018) 773-778.

14. Y. Lee, S. Lee, G. Seo, S. Paek, K.T. Cho, A.J. Huckaba, M. Calizzi, D.W. Choi, J.S. Park, D. Lee, H.J. Lee, A.M. Asiri, and M.K. Nazeeruddin, Efficient Planar Perovskite Solar Cells Using Passivated Tin Oxide as an Electron Transport Layer, Adv. Sci. 5 (2018) 1800130.

15. W. Ke, G. Fang, Q. Liu, L. Xiong, P. Qin, H. Tao, J. Wang, H. Lei, B. Li, J. Wan, G. Yang, and Y. Yan, Low-Temperature Solution-Processed Tin Oxide as an Alternative Electron Transporting Layer for Efficient Perovskite Solar Cells, J. Am. Chem. Soc. 137 (2015) 6730-6733.

16. S. Lin, B. Yang, X. Qiu, J. Yan, J. Shi, Y. Yuan, W. Tan, X. Liu, H. Huang, Y. Gao, and C. Zhou, Efficient and stable planar hole-transport-material-free perovskite solar cells using low temperature processed SnO2 as electron transport material, Org. Electron. 53 (2018) 235-241.

17. X. Qiu, B. Yang, H. Chen, G. Liu, Y. Liu, Y. Yuan, H. Huang, H. Xie, D. Niu, Y. Gao, and C. Zhou, Efficient, stable and flexible perovskite solar cells using two-step solution-processed SnO 2 layers as electron-transport-material, Org. Electron. 58 (2018) 126-132.

18. G. Yang, C. Chen, F. Yao, Z. Chen, Q. Zhang, X. Zheng, J. Ma, H. Lei, P. Qin, L. Xiong, W. Ke, G. Li, Y. Yan, and G. Fang, Effective Carrier-Concentration Tuning of SnO2 Quantum Dot Electron-Selective Layers for High-Performance Planar Perovskite Solar Cells, Adv. Mater. 30 (2018) 1706023.

19. J. Dagar, S. Castro-Hermosa, G. Lucarelli, F. Cacialli, and T.M. Brown, Highly efficient perovskite solar cells for light harvesting under indoor illumination via solution processed SnO 2 /MgO composite electron transport layers, Nano Energy 49 (2018) 290-299.

20. T. Bu, S. Shi, J. Li, Y. Liu, J. Shi, L. Chen, X. Liu, J. Qiu, Z. Ku, Y. Peng, J. Zhong, Y.B. Cheng, and F. Huang, Low-Temperature Presynthesized Crystalline Tin Oxide for Efficient Flexible Perovskite Solar Cells and Modules, ACS Appl. Mater. Interfaces 10 (2018) 14922-14929.

21. X. Liu, K.-W. Tsai, Z. Zhu, Y. Sun, C.-C. Chueh, and A.K.Y. Jen, A Low-Temperature, Solution Processable Tin Oxide Electron-Transporting Layer Prepared by the Dual-Fuel Combustion Method for Efficient Perovskite Solar Cells, Adv. Mater. Interfaces 3 (2016) 1600122.

22. L. Huang, X. Sun, C. Li, J. Xu, R. Xu, Y. Du, J. Ni, H. Cai, J. Li, Z. Hu, and J. Zhang, UV-Sintered Low-Temperature Solution-Processed SnO2 as Robust Electron Transport Layer for Efficient Planar Heterojunction Perovskite Solar Cells, ACS Appl. Mater. Interfaces 9 (2017) 21909-21920.

23. A.S. Subbiah, N. Mathews, S. Mhaisalkar, and S.K. Sarkar, Novel Plasma-Assisted Low-Temperature-Processed SnO2 Thin Films for Efficient Flexible Perovskite Photovoltaics, ACS Energy Lett. 3 (2018) 1482-1491.

24. C. Wang, L. Guan, D. Zhao, Y. Yu, C.R. Grice, Z. Song, R.A. Awni, J. Chen, J. Wang, X. Zhao, and Y. Yan, Water Vapor Treatment of Low-Temperature Deposited SnO2 Electron Selective Layers for Efficient Flexible Perovskite Solar Cells, ACS Energy Lett. 2 (2017) 2118-2124.

25. C. Wang, D. Zhao, C.R. Grice, W. Liao, Y. Yu, A. Cimaroli, N. Shrestha, P.J. Roland, J. Chen, Z. Yu, P. Liu, N. Cheng, R.J. Ellingson, X. Zhao, and Y. Yan, Low-temperature plasma-enhanced atomic layer deposition of tin oxide electron selective layers for highly efficient planar perovskite solar cells, J. Mater. Chem. A 4 (2016) 12080-12087.

26. J.-Y. Lam, J.-Y. Chen, P.-C. Tsai, Y.-T. Hsieh, C.-C. Chueh, S.-H. Tung, and W.-C. Chen, A stable, efficient textile-based flexible perovskite solar cell with improved washable and deployable capabilities for wearable device applications, RSC Adv. 7 (2017) 54361-54368.

27. W. Zhou, Y. Liu, Y. Yang, and P. Wu, Band Gap Engineering of SnO2 by Epitaxial Strain: Experimental and Theoretical Investigations, J. Phys. Chem. C 118 (2014) 6448-6453.

28. S.M. Ali, S.T. Hussain, S.A. Bakar, J. Muhammad, and N.u. Rehman, Effect of doping on the Structural and Optical Properties of SnO2Thin Films fabricated by Aerosol Assisted Chemical Vapor Deposition, J Phys. Conf. Ser. 439 (2013) 012013.

29. Z. Zhu, J. Ma, C. Luan, L. Kong, and Q. Yu, Structure and photoluminescence properties of epitaxial SnO2 films grown on α-Al2O3 (012) by MOCVD, J. Lumin. 131 (2011) 88-91.

30. F. García-Sánchez, B. Romero, D. Lugo-Muñoz, P. del, B. Arredondo, J. Liou, and A. Ortiz-Conde, Modelling solar cell S-shaped I-V characteristics with DC lumped-parameter equivalent circuits a review, Facta Univ. Ser. Electron. Energ. 30 (2017) 327-350.

31. K.T. Cho, S. Paek, G. Grancini, C. Roldán-Carmona, P. Gao, Y. Lee, and M.K. Nazeeruddin, Highly efficient perovskite solar cells with a compositionally engineered perovskite/hole transporting material interface, Energy Environ. Sci. 10 (2017) 621-627.

32. B. Ecker, H.-J. Egelhaaf, R. Steim, J. Parisi, and E. von Hauff, Understanding S-Shaped Current–Voltage Characteristics in Organic Solar Cells Containing a TiOx Interlayer with Impedance Spectroscopy and Equivalent Circuit Analysis, J. Phys. Chem. C 116 (2012) 16333-16337.

33. J.M. Themlin, R. Sporken, J. Darville, R. Caudano, J.M. Gilles, and R.L. Johnson, Resonant-photoemission study ofSnO2: Cationic origin of the defect band-gap states, Phys. Rev. B 42 (1990) 11914-11925.

34. J.P. Correa Baena, L. Steier, W. Tress, M. Saliba, S. Neutzner, T. Matsui, F. Giordano, T.J. Jacobsson, A.R. Srimath Kandada, S.M. Zakeeruddin, A. Petrozza, A. Abate, M.K. Nazeeruddin, M. Grätzel, and A. Hagfeldt, Highly efficient planar perovskite solar cells through band alignment engineering, Energy Environ. Sci. 8 (2015) 2928-2934.

35. Y. Zhang, N. Lin, Y. Li, X. Wang, H. Wang, J. Kang, R. Wilks, M. Bar, and R. Mu, The isotype ZnO/SiC heterojunction prepared by molecular beam epitaxy--A chemical inert interface with significant band discontinuities, Sci. Rep. 6 (2016) 23106.

36. V.M.L. Jiménez, G; Fernández, A.; Espinós, J. P.; Yubero, F.; González-Elipe, A. R.; Soriano, L.; Sanz, J. M. and Papaconstantopoulos, D. A. , Resonant photoemission characterization of SnO, Phys. Rev. B 60 (1999) 11171-11179.

37. F. Yang, J. Liu, H.E. Lim, Y. Ishikura, K. Shinokita, Y. Miyauchi, A. Wakamiya, Y. Murata, and K. Matsuda, High Bending Durability of Efficient Flexible Perovskite Solar

Cells Using Metal Oxide Electron Transport Layer, J. Phys. Chem. C 122 (2018) 17088-17095.

38. K.M.L. Freedy, P. M. and McDonnell, S., In-vacuo studies of transition metal dichalcogenide sythesis and layered material integration ECS Transactions 77 (2017) 11-25.

CHAPTER FOUR. MECHANISMS STUDY OF MENISCUS-GUIDED PEROVSKITE DEPOSITION FOR OPTOELECTRONIC DEVICES

4.1 Abstract

In order to realize scalable fabrication of perovskite optoelectronic devices, large area deposition techniques such as solution shearing must be realized and perfected. However, the mechanisms of fabrication processes are still not well studied in different solution shearing regimes. By monitoring the precursor species during crystallization process using *In-situ* Grazing Incidence Wide-Angle X-ray Scattering, the crystallization process in low shearing speed meniscus regime is proven to happen under lower supersaturation. The low supersaturation contributes to the bigger crystal size of thin film under lower shearing speed while high speed shearing results in higher supersaturation, causing thin films with small size crystals. Photodetectors with perovskite thin films coated at low shearing speed meniscus regime show much higher internal quantum efficiency because of the larger crystal domain size and uniform orientation inside of domains. This shows continuing study and rational design of the crystallization process is needed to push perovskite technology toward useful applications.

4.2 Introduction

Metal halide perovskite (MHPs) is one of the promising optoelectronic materials, which can be used to fabricate solar cells[1, 2], light emitting diode (LED)[3-6], field-effect transistor[7, 8], and photodetector[9-12] etc. MHPs exhibit high light absorbance coefficient[13] and long electron-hole diffusion length[13-15], which promote optoelectronic devices performance. Up to now, power conversion efficiency of perovskite solar cells has grown up to 25.2%[16]. Besides that, its solution-processed method decreases the fabrication cost compared with traditional optoelectronic materials. However, the commonly used thin film fabrication method, spin-coating is only able to coat uniform thin film with small area, from hundreds of millimeter to several square centimeters[17]. In order to scale up the fabrication process of perovskite optoelectronic devices through roll-to-roll process, thin films need fabricated on flexible substrate using large-area coating techniques.

There are many large-area coating techniques, such as ink jet printing, spray coating, slot die coating etc. Solution shearing will be chosen among all the large area fabrication methods in this manuscript since it can confine solvent evaporation in the edge of the droplet.[18] For solution shearing, for a solution system sheared at certain temperature, with liquid viscosity and surface tension, solvent evaporation rate and solute diffusion coefficient being the same, shearing speed is one of the main varieties we will focus on. There are two coating regimes featured by different shearing speed[19]. When shearing speed is sufficiently high, evaporation rate is significantly slower than the coating speed, so a liquid thin film will be dragged out first on substrates. In this situation, crystallization happens far away from solution meniscus, which is known as Landau-Levich (LL) regime[20]. In LL regime, blade moving is decoupled with solvent evaporation and crystallization, leading to crystallization performed by coating process is similar with that of spin coating process. When coating speed is sufficiently low enough such that, crystallization mainly happens in the solution meniscus, evaporative regime occurs[21-24]. In this regime, the solvent evaporation and crystallization happen in the similar time scale, which leads to solute crystalizes in meniscus, providing additional ways to control crystallization. So coating in evaporative regime is also called meniscus-guided deposition.

There are some researchers began to fabricate perovskite thin films using solution shearing or blade coating[25-30]. Perovskite thin film coated in evaporative regime has bigger crystals while for the reference spin coated sample, which would be similar with the sample coated in LL regime, crystal size is around several hundred nanometers. Li et al. reported perovskite arrays with micrometer width, centimeter length, parallel to shearing direction formed when thin film was coated in evaporative regime[27]. Kim et al. reported there are different morphology regimes when coating temperature and shearing speed changed and proposed it was because of supersaturation differences[31]. These results shown there are morphology and property differences when perovskite thin films are coated in different regimes.

However, crystallization processes and mechanisms in different shearing regimes, evaporative regime and LL regime are not well understood and proved. As we already know, uniform thin films with bigger crystal size or preferential orientation have lower election-hole recombination rate and better photovoltaics performance[32]. In order to fabricate thin film with desired optical and electrical properties, we need to understand crystallization mechanism in different shearing regimes.

Here, to study the crystallization mechanisms in different shearing regimes, we fabricated a series of samples by changing the shearing speed. Through *in-situ* crystallization process, shearing process in low shearing speed side show lower super-saturation compared with the process in high shearing speed. The low supersaturation contributes to the bigger crystal size of thin film while high speed shearing results in thin films with small size crystals. Photodetector with high internal quantum efficiency.

4.3 Results and discussion

As we talked above, shearing speed is one of the key parameters in solution shearing fabrication method. In order to understand the coating processes of thin films, flow dynamics in two coating regimes are need to be understood. In LL regime, perovskite crystallize along evaporation of the solvent while there are no affects from solution bulk. Since evaporation of the solvent happens after liquid thin film dragged out from solution bulk, the flow dynamics is similar with the case of spin coating method. While in evaporative regime, the flow dynamics is more complicated. Evaporation of the solvent in meniscus drive solution from bulk flow into meniscus, which dilute the concentrated solution in meniscus. On another side, there is concentration gradient of precursor species because of solvent evaporation. With high concentration in meniscus and low concentration in solution bulk, precursor species diffuse back to solution bulk. The complex dynamics makes it possible to control the supersaturation degree when samples are sheared in evaporative regime.

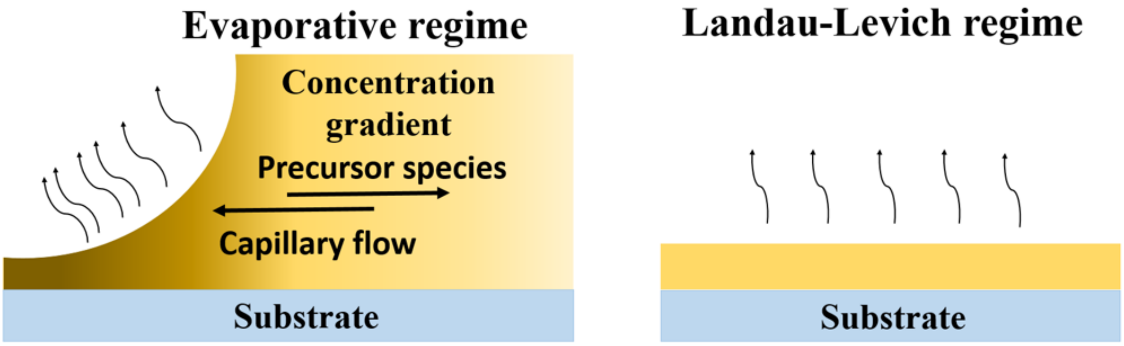

Figure 1 Diagram of flow dynamics in evaporative regime and LL regime.

To explore how could these different flow dynamics affect the thin films, we fabricated thin films under different shearing speed and characterized them. Substrate temperature was kept the same in order to keep other parameters consistent, such as evaporation rate of the solvent, diffusion coefficient of precursor species, liquid viscosity and surface tension, etc. Methylammonium lead iodide ($MAPbI_3$) thin films were fabricated at 150 ºC with different shearing speed, and optical microscope images are shown below in Figure 2, with scale bar of 0.1 mm. From the optical microscope images, we can observe clear differences with decrease of shearing speed. With the shearing speed of 3 mm/s, crystal domain is quite small with non-fully coverage among crystal domains. Along shearing speed get decreased, crystal domain gets bigger while fully coverage still cannot be achieved. When we keep lowering the shearing speed, huge oval-shaped crystal domain formed with fully coverage. SEM was used to observe these thin films in crystal level. The crystal size of sample sheared at 0.1 mm/s is huge compared with the samples sheared at higher shearing speed, shown in Figure S1.

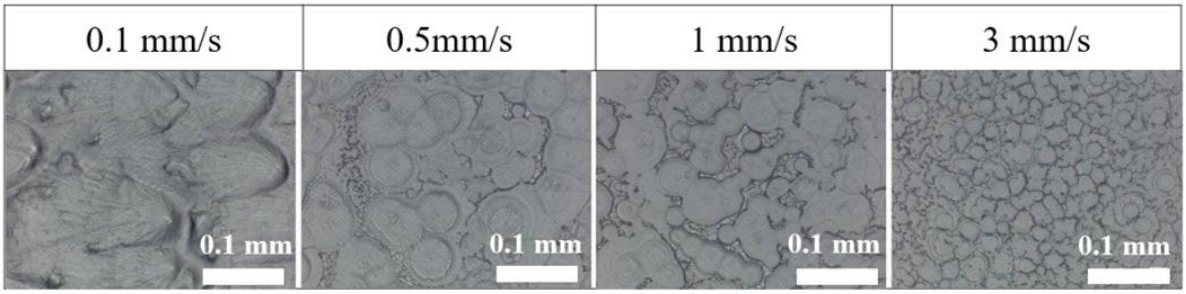

Figure 2 Optical microscope images of $MAPbI_3$ coated at 150 ºC with different shearing speed.

To understand these thin films comprehensively, some other characterizations have been done. Because the correlations between thickness of thin film and shearing speed are different in these two shearing regimes, thickness curve along shearing speed can be used to determine the shearing regime. When the coating speed is sufficiently low and evaporation rate of solvent near contact line is quite high, more solution flow into meniscus to make up the solvent evaporation, leading to more solute accumulate onto the thin film. So lower coating speed in evaporative regime will lead to thicker thin-film. There is a model to descript the correlation between thickness and shearing speed:

$$h \propto 1/\nu$$

where h is the thickness of the thin film, and ν is the shearing speed. Thicknesses of thin films were measured by profilometer, and plotted as Figure 3(a). The lowest shearing speed, 0.1 mm/s is in the low speed end of evaporative regime, 1 mm/s is in the high speed end of evaporative regime, while 3 mm/s is in transition area between evaporative regime and LL regime. UV-Vis results are consistent with thickness results. Absorption increased along the shearing speed decreased, until the thin film is thick enough to absorb all the light between 400 nm to 800 nm, shown in Figure 3(b). In Figure 3(c), photo luminescence shows all the samples have strong $MAPbI_3$ peaks around 760 nm.

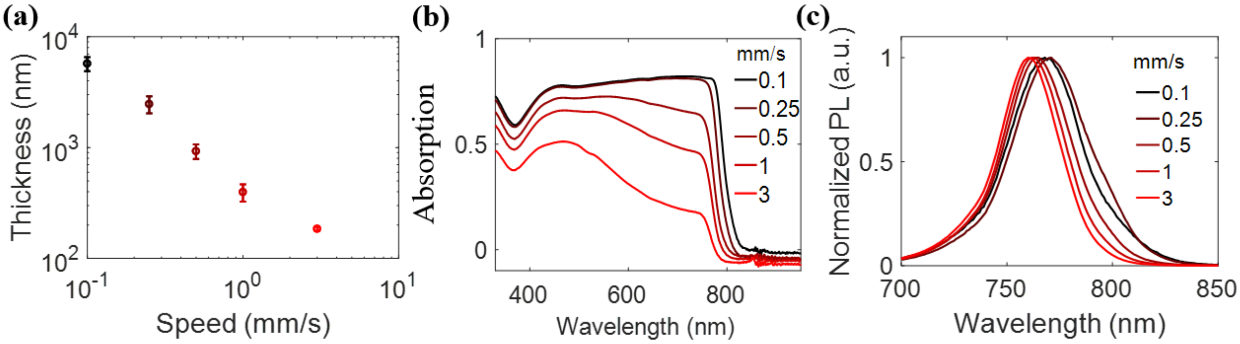

Fig. 3 (a) Thickness (b) Absorption (c) Photoluminance of thin films coated at 150 °C with different shearing speeds.

So far, there has been no systematic study about what is the reason for the different crystallization processes under different shearing speed. In order to study crystallization processes, we used

GIWAXS which is good at detecting crystal structure, combining with the *in-situ* solution shearing setup, to capture crystallization processes. With static substrate and X-ray source, the detector keeps collecting the crystal structure information from the same spot of the sample during crystallization process.

Bragg's equation is the principle of GIWAXS, like one dimension XRD. When the crystal has long range order, GIWAXS pattern will have bright clear peaks. If there is short range order, the pattern will show broader peaks. In perovskite solution, some precursor species will form between perovskite and solvent molecules[33-37], which will show up in GIWAXS pattern as broad peaks. If perovskite crystal is random oriented, rings show up in the GIWAXS pattern since Bragg's equation can be satisfied in different angles. If the crystal is oriented in the area X-ray is able to detect, Bragg's equation only can be satisfied in certain angle, which mean only certain dots will show up in rings. If the crystal is aligned, not all the dots can be detected. Here we used micro beam as X-ray source, with size of 20 μm. Considering the small beam size and only part of crystals can be detected by X-ray, pattern can only show a few dots when the crystal size is large even if not all the crystals are aligned.

First we analyzed the crystallization process under higher shearing speed, 1 mm/s. Shown in Figure 4 (top), at beginning of crystallization, the broad ring appeared, which indicates the formation of precursor species. Then perovskite crystal peaks begin to show up while the brightness of precursor species peak decreased. At the end of crystallization process, precursor species peak disappeared and perovskite rings are brightest. The *in-situ* movie shows that random oriented perovskite crystalized from precursor structure when the shearing speed is higher. Compared with the process in higher shearing speed, crystallization process in lower shearing speed is much different, for example the sample sheared at 0.1 mm/s. Shown in Figure 4 (bottom), at beginning of crystallization process, there is no precursor species peak showed up. Then only a few of dots became brighter, which means big crystal formed during lower shearing speed crystallization process based on the analysis above. This is also consistent with the thin film morphology we observed. Based on this *in-situ* information, the shearing process under lower shearing speed is a great method to control the crystallization process to achieve big crystal directly from solution.

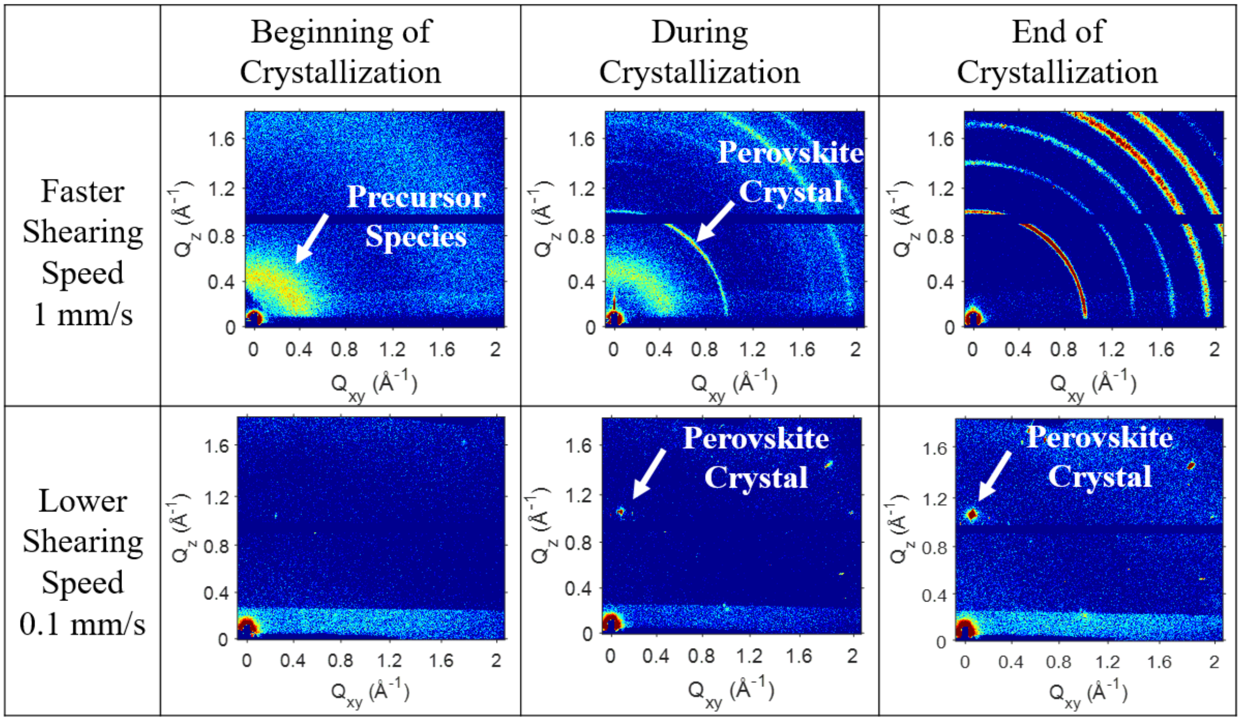

Fig. 4 *in-situ* GIWAXS for higher shearing speed (1 mm/s) and lower shearing speed (0.1 mm/s)

We integrated precursor species and perovskite crystal peak in *in-situ* movies and the results are shown in Figure 5(a). For crystallization process sheared under higher shearing speed, the precursor species peak decreased along the perovskite peak increased, while for crystallization process under lower shearing speed, precursor species peak is ignorable compared with perovskite peak. The precursor species are complex structure combining solvent and solute molecules. Under high supersaturation degree, the ratio of solute molecules to solvent molecules become much higher compared with low supersaturation degree, then the complex is more likely to form short-order structure which can be detected by GIWAXS.

As we knew, supersaturation is the driving force for nucleation and growth. Nucleation has a thermodynamic barrier since free energy will only decrease when the radius of nuclei reaches the critical radius. After the critical radius, growth happens driven by free energy decrease when the radius increases, which makes growth is easier to happen than nucleation thermodynamically. When the solvent is under low supersaturation degree, there is an equilibrium of crystal formation and dispersion because the change of Gibbs free energy is not high enough to overcome the surface energy. So only crystal growth can happen in this region. When the supersaturation degree is higher, the change of Gibbs free energy will be large enough to drive nucleation, which lead to high nucleation density and small crystals, shown in Figure 5(a). So lower supersaturation degree is the key to achieve low nucleation density and bigger crystals, shown in Figure 5(d).

In lower shearing speed, solvent evaporation happens in the meniscus, capillary flow will be the complementary flow for the evaporated solvent, which can help with controlling supersaturation degree. The crystals formed under lower shearing speed will have bigger grain size compared with crystals formed under higher shearing speed, where supersaturation degree is much higher during crystallization process.

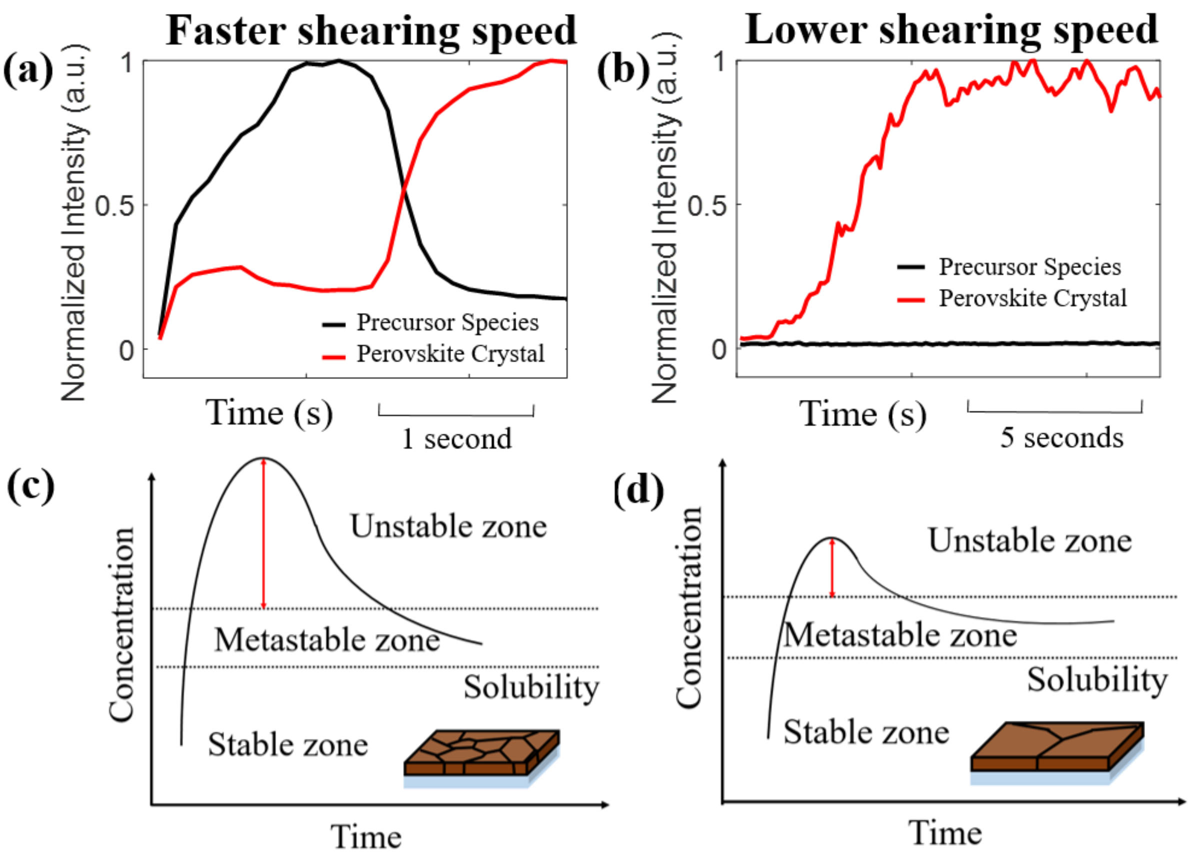

Fig. 5 (a) Crystallization process diagram for higher shearing speed, 1 mm/s and (b) lower shearing speed, 0.1 mm/s (c) Normalized peak intensity of solvent species and perovskite crystal for thin film sheared at 1 mm/s (d) 0.1 mm/s

In order to explore the impact of different morphology on optoelectronic devices, we fabricated photodetector with perovskite thin film sheared at different shearing speed, 1 mm/s and 0.1 mm/s. After perovskite shearing, nm of gold was deposited on top of perovskite thin film as conduct with channel length of 100 μm. The structure of photodetector is shown in Figure 5(a). Light current and dark current of these two devices are plotted in Figure 5(b). The current of J-V curve of the photodetector with thin film sheared at 0.1 mm/s is two magnitudes higher than the photodetector with thin film sheared at 1 mm/s, while there is only small difference in absorbance between thin films sheared at different shearing speed. We calculated internal quantum efficiency (IQE) of two samples, lower shearing speed sample demonstrated much higher IQE, shown in Figure 5(c).

The reason of high IQE for photodetector with thin film sheared at low shearing speed may be from low trap sites of the thin film. Crystal domain has uniform orientation has low trap density and recombination rate. The thin film sheared at 0.1 mm/s has large crystal domain, and GIWXS proved the crystals are aligned in the crystal domain. This may be the reason for the high IQE of photodetector with thin film sheared at 0.1 mm/s.

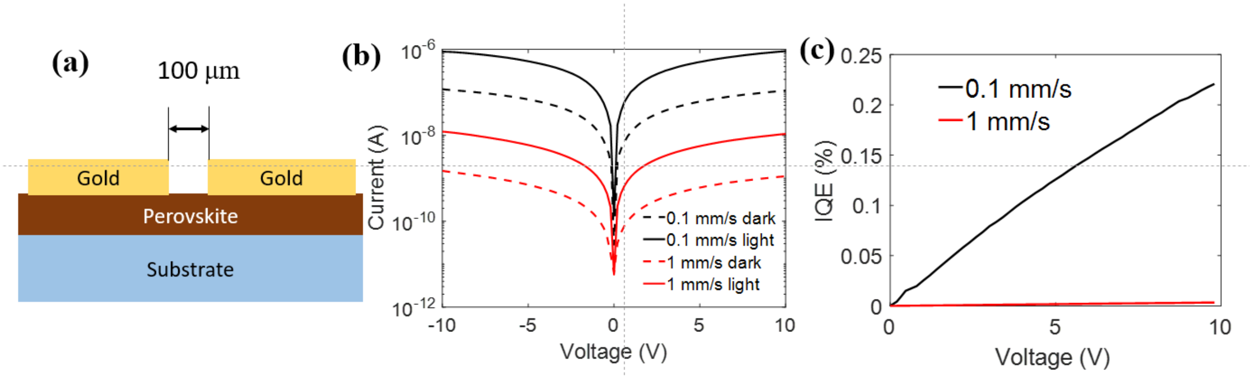

Fig. 5 (a) Structure of photodetector (b) J-V curve of photodetector fabricated with perovskite thin film sheared at 1 mm/s and 0.1 mm/s (c) IQE of photodetector fabricated with perovskite thin film sheared at 1 mm/s and 0.1 mm/s

In summary, a serious of samples has been fabricated and the thin film sheared at lower shearing speed has bigger crystals. *In-situ* GIWAXS was used to capture the crystal structure during crystallization processes. The scattering signal from crystallization process under higher shearing speed shows short-ordered precursor species, which is intermediate structure formed between solute and solvent molecules when the supersaturation degree is high. The crystallization process in low shearing speed does not give the precursor species, which prove the crystallization happens under lower degree of supersaturation. The low supersaturation degree contributes to the bigger crystal size of thin film under lower shearing speed. We are able to control perovskite crystallization by controlling the supersaturation degree. Photodetectors with perovskite thin films coated at low shearing speed meniscus regime show much higher internal quantum efficiency because of the larger crystal domain size and uniform orientation inside of domains.

4.4 Methods

Photodetector fabrication

The patterned ITO substrates were cleaned by sonicating sequentially in Hellmanex III detergent, deionized water, and ethanol in an ultrasonic cleaner, rinsed with acetone and IPA, and treated by ultraviolet ozone plasma for 10 minutes. A precursor solution of perovskite $MAPbI_3$ with a 1.8 M concentration was prepared by dissolving 705.34 mg PbI_2 (Sigma), 30.23 mg CH_3NH_3I (MAI, Dyesol) in 1 mL of Dimethylacetamide (DMAc, Sigma). The solution was stirred on a hotplate at 60 °C for several hours until all solids were dissolved, then was filtered with 0.45 μL PTFE filter. Small amount of perovskite solution was dropped right underneath the blade when the stage was heated up to certain temperature. The blade was controlled by the linear controller to shear solution at certain shearing speed. The thin films were annealed at the stage for 10 minutes after shearing process. After the deposition of perovskite thin film, a nm of Au thin film was deposited by physical vapor deposition method as contact, with the channel width as 100 μm.

Characterization

Optical Microscope: Optical images were acquired on a Zeiss Axio A.1 Microscope with 5x, 10x, 20x, 50x objective lenses under cross-polarized light.

Profilorometer: Thickness of thin films are measured by DektakXT Surface Profile Measuring System from Bruker with force of 1g. Thin films were scratched to expose substrate, and thicknesses were calculated from subtracting height of exposed substrate from the height of film surface. Average thickness were obtained from three different positions of the same sample.

UV-Vis: UV/Vis/NIR Lambda 950 S spectrometer from Perkin Elmer with an integrating sphere was used to measure UV-Vis spectra of the SnO_2 thin films. Absorbance of film has been calculated by subtracting transmission and reflection from 1.

PL: Photoluminescence (PL) spectra were collected on a PTI Quantamaster 400 (QM-400) system.

GIWAXS: GIWAXS was performed at D-1 beamline at Cornell High Energy Synchrotron Source (CHESS) using X-rays with a wavelength of 1.162 Å. Reflections were collected using a Pilatus 200k 2D pixel array detector (Dectris) 160 nm away from sample. The 2D diffraction was processed and plotted by GIXSGUI.

Power Meter: Light intensity was measured by PM16-120, an USB Power Meter with standard photodiode silicon sensor. The actual power was calibrated based on efficiency spectrum.

4.5 Supplement information

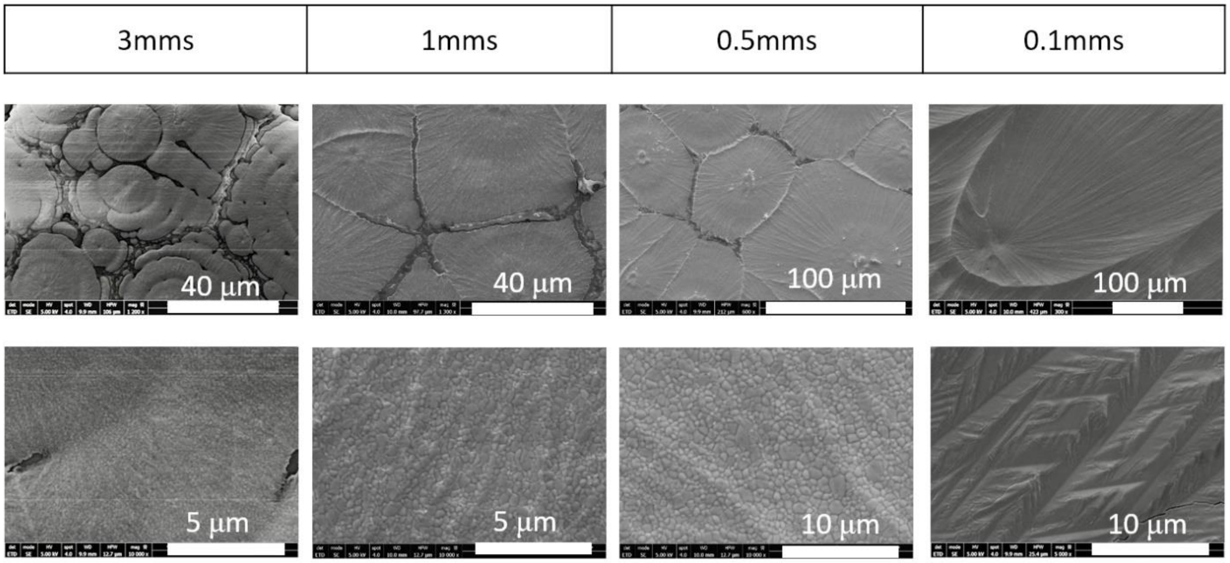

Figure S1 SEM of samples sheared at different shearing speed

4.6 Reference

1. S. Bai, P. Da, C. Li, Z. Wang, Z. Yuan, F. Fu, M. Kawecki, X. Liu, N. Sakai, J.T. Wang, S. Huettner, S. Buecheler, M. Fahlman, F. Gao, and H.J. Snaith, Planar perovskite solar cells with long-term stability using ionic liquid additives, Nature 571 (2019) 245-250.
2. Q. Jiang, Y. Zhao, X. Zhang, X. Yang, Y. Chen, Z. Chu, Q. Ye, X. Li, Z. Yin, and J. You, Surface passivation of perovskite film for efficient solar cells, Nature Photonics 13 (2019) 460-466.
3. Q. Van Le, H.W. Jang, and S.Y. Kim, Recent Advances toward High-Efficiency Halide Perovskite Light-Emitting Diodes: Review and Perspective, Small Methods 2 (2018) 1700419.

4. Y. Wei, Z. Cheng, and J. Lin, An overview on enhancing the stability of lead halide perovskite quantum dots and their applications in phosphor-converted LEDs, Chem Soc Rev 48 (2019) 310-350.
5. L. Zhang, Y. Liu, Z. Yang, and S. Liu, Two dimensional metal halide perovskites: Promising candidates for light-emitting diodes, Journal of Energy Chemistry 37 (2019) 97-110.
6. Q. Zhang, M.M. Tavakoli, L. Gu, D. Zhang, L. Tang, Y. Gao, J. Guo, Y. Lin, S.F. Leung, S. Poddar, Y. Fu, and Z. Fan, Efficient metal halide perovskite light-emitting diodes with significantly improved light extraction on nanophotonic substrates, Nat Commun 10 (2019) 727.
7. W. Yu, F. Li, L. Yu, M.R. Niazi, Y. Zou, D. Corzo, A. Basu, C. Ma, S. Dey, M.L. Tietze, U. Buttner, X. Wang, Z. Wang, M.N. Hedhili, C. Guo, T. Wu, and A. Amassian, Single crystal hybrid perovskite field-effect transistors, Nat Commun 9 (2018) 5354.
8. B.Y. Satyaprasad P. Senanayak, Tudor H. Thomas, Nadja Giesbrecht, Wenchao Huang, Eliot Gann, Bhaskaran Nair, Karl Goedel, Suchi Guha, Xavier Moya, Christopher R. McNeill, Pablo Docampo, Aditya Sadhanala, Richard H. Friend and Henning Sirringhaus, Understanding charge transport in lead iodide perovskite thin-film field-effect transistors, Sci. Adv. 3 (2017)
9. A.A. Khan, Z. Yu, U. Khan, and L. Dong, Solution Processed Trilayer Structure for High-Performance Perovskite Photodetector, Nanoscale Res Lett 13 (2018) 399.
10. J. Miao and F. Zhang, Recent progress on highly sensitive perovskite photodetectors, Journal of Materials Chemistry C 7 (2019) 1741-1791.

11. M. Zhang, F. Zhang, Y. Wang, L. Zhu, Y. Hu, Z. Lou, Y. Hou, and F. Teng, High-Performance Photodiode-Type Photodetectors Based on Polycrystalline Formamidinium Lead Iodide Perovskite Thin Films, Sci Rep 8 (2018) 11157.

12. D.H. Chun, Y.J. Choi, Y. In, J.K. Nam, Y.J. Choi, S. Yun, W. Kim, D. Choi, D. Kim, H. Shin, J.H. Cho, and J.H. Park, Halide Perovskite Nanopillar Photodetector, ACS Nano 12 (2018) 8564-8571.

13. S.D. Stranks, G.E. Eperon, G. Grancini, C. Menelaou, M.J.P. Alcocer, T. Leijtens, L.M. Herz, A. Petrozza, and H.J. Snaith, Electron-Hole Diffusion Lengths Exceeding 1 Micrometer in an Organometal Trihalide Perovskite Absorber, Science 342 (2013) 341-344.

14. Y. Wang, Y. Zhang, P. Zhang, and W. Zhang, High intrinsic carrier mobility and photon absorption in the perovskite CH3NH3PbI3, Phys Chem Chem Phys 17 (2015) 11516-20.

15. A.V. Shi D, Comin R, Yuan M, Alarousu E, Buin A, Chen Y, Hoogland S, Rothenberger A, Katsiev K, Losovyj Y, Zhang X, Dowben PA, Mohammed OF, Sargent EH, Bakr OM, Solar cells Low trap-state density and long carrier diffusion in organolead trihalide perovskite single crystals, Science 347 (2015) 519.

16. X. Liu, K.-W. Tsai, Z. Zhu, Y. Sun, C.-C. Chueh, and A.K.Y. Jen, A Low-Temperature, Solution Processable Tin Oxide Electron-Transporting Layer Prepared by the Dual-Fuel Combustion Method for Efficient Perovskite Solar Cells, Adv. Mater. Interfaces 3 (2016) 1600122.

17. Z. Yang, S. Zhang, L. Li, and W. Chen, Research progress on large-area perovskite thin films and solar modules, Journal of Materiomics 3 (2017) 231-244.

18. Y. Diao, L. Shaw, Z. Bao, and S.C.B. Mannsfeld, Morphology control strategies for solution-processed organic semiconductor thin films, Energy Environ. Sci. 7 (2014) 2145-2159.

19. X. Gu, L. Shaw, K. Gu, M.F. Toney, and Z. Bao, The meniscus-guided deposition of semiconducting polymers, Nat Commun 9 (2018) 534.

20. H. Yang and P. Jiang, Large-scale colloidal self-assembly by doctor blade coating, Langmuir 26 (2010) 13173-82.

21. G. Jing, H. Bodiguel, F. Doumenc, E. Sultan, and B. Guerrier, Drying of colloidal suspensions and polymer solutions near the contact line: deposit thickness at low capillary number, Langmuir 26 (2010) 2288-93.

22. F. Doumenc, J.B. Salmon, and B. Guerrier, Modeling Flow Coating of Colloidal Dispersions in the Evaporative Regime: Prediction of Deposit Thickness, Langmuir 32 (2016) 13657-13668.

23. R. Janneck, F. Vercesi, P. Heremans, J. Genoe, and C. Rolin, Predictive Model for the Meniscus-Guided Coating of High-Quality Organic Single-Crystalline Thin Films, Adv Mater 28 (2016) 8007-8013.

24. C. Loussert, F. Doumenc, J.B. Salmon, V.S. Nikolayev, and B. Guerrier, Role of Vapor Mass Transfer in Flow Coating of Colloidal Dispersions in the Evaporative Regime, Langmuir 33 (2017) 14078-14086.

25. Y. Deng, Q. Wang, Y. Yuan, and J. Huang, Vividly colorful hybrid perovskite solar cells by doctor-blade coating with perovskite photonic nanostructures, Materials Horizons 2 (2015) 578-583.

26. M. Yang, Z. Li, M.O. Reese, O.G. Reid, D.H. Kim, S. Siol, T.R. Klein, Y. Yan, J.J. Berry, M.F.A.M. van Hest, and K. Zhu, Perovskite ink with wide processing window for scalable high-efficiency solar cells, Nature Energy 2 (2017) 17038.

27. J. Li, Y. Liu, X. Ren, Z. Yang, R. Li, H. Su, X. Yang, J. Xu, H. Xu, J.-Y. Hu, A. Amassian, K. Zhao, and S.F. Liu, Solution Coating of Superior Large-Area Flexible Perovskite Thin Films with Controlled Crystal Packing, Advanced Optical Materials 5 (2017) 1700102.

28. Y. Deng, Q. Dong, C. Bi, Y. Yuan, and J. Huang, Air-Stable, Efficient Mixed-Cation Perovskite Solar Cells with Cu Electrode by Scalable Fabrication of Active Layer, Advanced Energy Materials 6 (2016) 1600372.

29. M. He, B. Li, X. Cui, B. Jiang, Y. He, Y. Chen, D. O'Neil, P. Szymanski, M.A. Ei-Sayed, J. Huang, and Z. Lin, Meniscus-assisted solution printing of large-grained perovskite films for high-efficiency solar cells, Nat Commun 8 (2017) 16045.

30. H. Wu, C. Zhang, K. Ding, L. Wang, Y. Gao, and J. Yang, Efficient planar heterojunction perovskite solar cells fabricated by in-situ thermal-annealing doctor blading in ambient condition, Organic Electronics 45 (2017) 302-307.

31. M.K. Kim, H.S. Lee, S.R. Pae, D.-J. Kim, J.-Y. Lee, I. Gereige, S. Park, and B. Shin, Effects of temperature and coating speed on the morphology of solution-sheared halide perovskite thin-films, J. Mater. Chem. A 6 (2018) 24911-24919.

32. B.J. Foley, S. Cuthriell, S. Yazdi, A.Z. Chen, S.M. Guthrie, X. Deng, G. Giri, S.-H. Lee, K. Xiao, B. Doughty, Y.-Z. Ma, and J.J. Choi, Impact of Crystallographic Orientation Disorders on Electronic Heterogeneities in Metal Halide Perovskite Thin Films, Nano Lett. 18 (2018) 6271-6278.

33. Y. Guo, K. Shoyama, W. Sato, Y. Matsuo, K. Inoue, K. Harano, C. Liu, H. Tanaka, and E. Nakamura, Chemical Pathways Connecting Lead(II) Iodide and Perovskite via Polymeric Plumbate(II) Fiber, J. Am. Chem. Soc. 137 (2015) 15907-14.

34. Q. Hu, L. Zhao, J. Wu, K. Gao, D. Luo, Y. Jiang, Z. Zhang, C. Zhu, E. Schaible, A. Hexemer, C. Wang, Y. Liu, W. Zhang, M. Gratzel, F. Liu, T.P. Russell, R. Zhu, and Q. Gong, In situ dynamic observations of perovskite crystallisation and microstructure evolution intermediated from [PbI6](4-) cage nanoparticles, Nat Commun 8 (2017) 15688.

35. D.P. Nenon, J.A. Christians, L.M. Wheeler, J.L. Blackburn, E.M. Sanehira, B. Dou, M.L. Olsen, K. Zhu, J.J. Berry, and J.M. Luther, Structural and chemical evolution of methylammonium lead halide perovskites during thermal processing from solution, Energy Environ. Sci. 9 (2016) 2072-2082.

36. A. Sharenko, C. Mackeen, L. Jewell, F. Bridges, and M.F. Toney, Evolution of Iodoplumbate Complexes in Methylammonium Lead Iodide Perovskite Precursor Solutions, Chem. Mater. 29 (2017) 1315-1320.

37. S.J. Yoon, K.G. Stamplecoskie, and P.V. Kamat, How Lead Halide Complex Chemistry Dictates the Composition of Mixed Halide Perovskites, J Phys Chem Lett 7 (2016) 1368-73.

CHAPTER FIVE. CONCLUSION

Perovskite is one of the most promising materials in solar industry. In this thesis, we solved two challenges in order to commercialized perovskite solar cells by high-throughput roll-to-roll method.

The first challenge is low temperature processing of all device layers are need to be realized. The most commonly used electron transporting layer in high-performance perovskite solar cells are TiO_2 thin films and SnO_2 thin film processed at high temperature (450 °C and 180 °C respectively). Therefore, I designed the low temperature processes to fabricate TiO_x using another kind of precursor titanium isopropoxide, which is easier to hydrolyze compared with commonly used precursor. We also developed low temperature process for SnO_2 thin film by treating the precursor thin film using UVO_3. Flexible solar cells fabricated with these thin films with decent power conversion efficiency are demonstrated, and these flexible solar cells are able to remain 80% - 90% power conversion efficiency after hundreds of bending cycles.

The second challenge is that large area deposition techniques such as solution shearing is realized and perfected. We fabricated a serious of samples and found out the thin film sheared at lower shearing speed has bigger crystals. In order to study the mechanisms of fabrication processes under different solution shearing speed, we used In-situ Grazing Incidence Wide-Angle X-ray Scattering, which is a useful tool to analysis the crystal structure, to capture the crystallization. The scattering signal from crystallization process under higher shearing speed shows short-ordered precursor species, which is intermediate structure formed between solute and solvent molecules when the supersaturation is high. The crystallization process in low shearing speed does not give the precursor species, which prove the crystallization happens under lower supersaturation. The low supersaturation contributes to the bigger crystal size of thin film under lower shearing speed. Photodetectors with perovskite thin films coated at low shearing speed meniscus regime show much higher internal quantum efficiency because of the larger crystal domain size and uniform orientation inside of domains. This shows continuing study and rational design of the crystallization process is needed to push perovskite technology toward useful applications.

Now with these solutions we developed for roll-to-roll process, large-area flexible optoelectronic devices are able to be fabricated. Here are some recommendations for future work.

For scalability of perovskite thin film, shearing speed can be optimized because the shearing speed we used in this study is too low for industrial fabrication. We already fabricated thin film with desired properties, but with the 0.1 mm/s shearing speed, it is hard to coat the thin film efficiently in industry. As we know, substrate temperature along shearing speed decide the coating regime of solution shearing. If we want to fabricate thin film under the same low degree of supersaturation at higher shearing speed, we need to reduce the solvent evaporation rate, which mean lower the substrate temperature. By optimizing substrate temperature and shearing speed, we are able to find the optimized parameters to fabricate perovskite thin film with desired properties under low supersaturation degree.

Furthermore, we could also combine the low-temperature thin film fabrication processes and solution shearing together to achieve roll-to-roll fabrication method to fabricate large-area optoelectronic devices. Commercialization of perovskite optoelectronic devices will be achieved.